EPJ manuscript No.
(will be inserted by the editor)

Quest for understanding hadrons at low energies: Monte Carlo tools vs. experimental data

Working Group on Radiative Corrections and Monte Carlo Generators for Low Energies

P. Beltrame[1], H. Czyż[2 13], A. Denig[1], S. Eidelman[3], G. V. Fedotovich[3 4], A. Grzelińska[5], S. E. Müller[1], W. Kluge[6], J. H. Kühn[7], F. Nguyen[8], G. Pakhlova[9], G. Pancheri[10], O. Shekhovtsova[10], C. P. Shen[11], A. L. Sibidanov[3], G. Venanzoni[10 13], P. Wang[12], and C. Z. Yuan[12]

[1] Institut für Kernphysik, Johannes Gutenberg - Universität Mainz, Mainz, Germany
[2] Institute of Physics, University of Silesia, PL-40007 Katowice, Poland
[3] Budker Institute of Nuclear Physics, 630090 Novosibirsk, Russia
[4] Novosibirsk State University, 630090 Novosibirsk, Russia
[5] Institute of Nuclear Physics Polish Academy of Sciences, PL-31342 Cracow, Poland
[6] Institut für Experimentelle Kernphysik, Universität Karlsruhe, Karlsruhe, Germany
[7] Institut für Theoretische Teilchenphysik, Universität Karlsruhe, D-76128 Karlsruhe, Germany.
[8] Dipartimanto di Fisica dell'Università "Roma Tre" and INFN Sezione di Roma Tre, Roma, Italy
[9] Institute of Theoretical and Experimental Physics, Moscow, Russia
[10] Laboratori Nazionali di Frascati dell'INFN, Frascati, Italy
[11] Univ. of Hawaii, USA
[12] Institute of High Energy Physics, Beijing, China
[13] Working group convener

Received: date / Revised version: date

Abstract. Insert your abstract here.

PACS. PACS-key discribing text of that key – PACS-key discribing text of that key

1 Introduction

introduction [1]

2 Luminosity

luminosity [2]

3 Scan

scan

4 Radiative return

4.1 History and evolution of the radiative return in precision physics

The idea to use *Initial State Radiation* in order to measure hadronic cross sections from the threshold of a reaction up to the centre-of-mass (c.m.) energy of colliders with fixed energies $\sqrt{s}$, to reveal reaction mechanisms and to search for new mesonic states consists in exploiting the process $e^+e^- \to hadrons + n\gamma$ to reduce the c.m. energy of the colliding electrons and positrons and consequently the mass squared $M_{had}^2 = s - 2\sqrt{s}\, E_\gamma$ of the hadronic system in the final state by emitting one or more photons. The method is particularly well suited for the modern meson factories like $DA\Phi NE$ (detector $KLOE$) running at the ϕ-resonance, *BEPCII* (detector *BESIII*), commissioned in 2008, at the J/ψ and $\psi(2S)$-resonances, *PEP-II* (detector *BABAR*) and *KEKB* (detector *Belle*) at the $\Upsilon(4S)$-resonance with their high luminosities which compensate for the α/π suppression of the emission of a photon. $DA\Phi NE$, *BEPCII*, *PEP-II* and *KEKB* cover the regions in M_{had} up to 1.02 GeV, up to 3.8 (maximally 4.6) GeV and up to 10.6 GeV, respectively (restricted for the latter actually up to 4–5 GeV if hard photons are detected). A big advantage of the *ISR* method is the low point-to-point systematic errors of the hadronic energy spectra because the luminosity, the energy of the electrons and positrons and many other contributions to the detection efficiencies are determined once for the whole spectrum. As a consequence, the overall normalization error is the same for all energies of the hadronic system. The term *Radiative return* alternately used for *ISR* refers to the appearance of pronounced resonances (e.g. $\rho, \omega, \phi, J/\psi, Z$) with energies below the collider energy. Reviews and updated results can be found in the Proceedings of the International Workshops in Pisa (2003) [3], Nara (2004) [4], Novosibirsk (2006) [5], Pisa (2006) [6], Frascati (2008) [7], Novosibirsk (2008) [8].

Calculations of *ISR* date back to the sixties-seventies of the 20^{th} century. For example, photon emission for muon pair production in electron-positron collisions has been calculated in Ref. [9], for the 2π-final state in Ref. [10,11], resonances (ρ, ω, ϕ) have been implemented in Ref. [11], the excitation of $\psi(3100)$ and $\psi'(3700)$ in Ref. [12], and the possibility to determine the pion form factor was discussed in Ref. [13]. The application of *ISR* to the new high luminosity meson factories, originally aimed at the determination of the hadronic contribution to vacuum polarization, more specifically the pion form factor, has materialized in the late nineties. Early calculations of *ISR* for the colliders *DAΦNE*, *PEP-II*, *KEKB* can be found in [14–17]. In Ref. [18] calculations of radiative corrections for pion and kaon production below energies of 2 GeV have been reported. An impressive example of *ISR* is the *Radiative Return* to the region of the Z-resonance at *LEP 2* with collider energies around 200 GeV [19–22] (see Fig. 1).

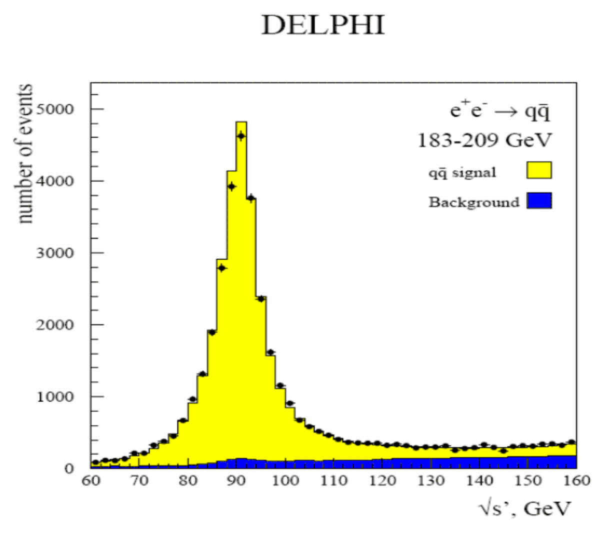

Fig. 1. The reconstructed distribution of $e^+e^- \to q\bar{q}$ events as a function of the invariant mass of the quark-antiquark system. The data has been taken for a collider energy range of 182 - 209 GeV. The prominent peak around 90 GeV represents the Z-resonance, populated after emission of photons in the initial state [20].

ISR became a powerful tool for the analysis of experiments at low and intermediate energies with the development of *EVA-PHOKHARA*, a Monte Carlo event generator which is user friendly, flexible and easy to implement into the software of the existing detectors [23–39].

EVA and its successor *PHOKHARA* allow to simulate the process $e^+e^- \to hadrons + \gamma$ for a variety of exclusive final states. As a starting point *EVA* was constructed [23] to simulate leading order *ISR* and *FSR* for the $\pi^+\pi^-$ channel, additional soft and collinear ISR was included on the basis of structure functions taken from [40]. Subsequently *EVA* was extended to include the four-pion state [24], however, without *FSR*. Neglecting *FSR* and radiative corrections, i. e. including one-photon emission from the initial state only, the cross section for the radiative return can be cast into the product of a radiator function $H(M^2_{had}, s)$ and the cross section $\sigma(M^2_{had})$ for the reaction $e^+e^- \to hadrons$:

$$s\, d\sigma(e^+e^- \to hadrons\ \gamma)/dM^2_{had} = \sigma(M^2_{had})\ H(M^2_{had}, s).$$

However, for a precise evaluation of $\sigma(M^2_{had})$ the leading logarithmic approximation inherent in *EVA* is insufficient. Therefore, in the next step, the exact one-loop correction to the *ISR* process was evaluated analytically, first for large angle photon emission [25], then for arbitrary, including collinear configurations [26]. This was and is one of the key ingredients of the generator called *PHOKHARA* [27,28], which also includes soft and hard real radiation, evaluated using exact matrix elements formulated within the framework of helicity amplitudes [27]. *FSR* in *NLO* approximation was addressed in [29] and incorporated in [30,31]. The importance of the charge asymmetry, a consequence of interference between *ISR* and *FSR* amplitudes, for a test of the (model dependent) description of *FSR* has been emphasized already in Ref.[23] and was further studied in [31].

Subsequently the generator was extended to allow the generation of many more channels with mesons, like K^+K^-, $K^0\bar{K}^0$, $\pi^+\pi^-\pi^0$, an improved description of the 4π modes [32,33] and improvements in the description of *FSR* for the $\mu^+\mu^-$ channel [30,31]. Also the nucleon channels $p\bar{p}$ and $n\bar{n}$ were implemented [34] and it was demonstrated that the separation of electric and magnetic proton form factors is feasible for a wide energy range. In fact, for the case of $\Lambda\bar{\Lambda}$ and including the polarization sensitive weak decay of Λ into the simulation, it was shown that even the relative phase between the two independent form factors could be disentangled [35].

Starting already with [41] various improvements were made to include the direct decay $\phi \to \pi^+\pi^-\gamma$ as a specific aspect of *FSR* into the generator, a contribution of specific importance for data taken on top of the ϕ resonance.

This was further pursued in the event generators *FEVA* and *FASTERD* based on *EVA-PHOKHARA*. *FEVA* includes the effects of the direct decay $\phi \to \pi^-\pi^+\gamma$ and the decay via the ρ-resonance $\phi \to \rho^\pm\pi^\mp \to \pi^-\pi^+\gamma$ [42–44]. The code *FASTERD* takes into account *Final State Radiation* in the frameworks of both Resonance Perturbation Theory and sQED, *Initial State Radiation* and their interference and the direct decays $e^+e^- \to \phi \to (f_o; f_o + \sigma)\gamma \to \pi^+\pi^-\gamma$, $e^+e^- \to \phi \to \rho^\pm\pi^\mp \to \pi^+\pi^-\gamma$ and $e^+e^- \to \rho \to \omega\pi^o \to \pi^o\pi^o\gamma$ [45], with the possibility to include additional models.

EVA-PHOKHARA was applied for the first time to an experiment to determine the cross section $e^+e^- \to \pi^+\pi^-$

from the reaction threshold up to the maximum energy of the collider with the detector *KLOE* at *DAΦNE* [46–70] (Section 4.4.1). The motivation was the determination of the 2π final state contribution to the hadronic vacuum polarization.

The determination of the hadronic contribution to the vacuum polarization, which arises from the coupling of virtual photons to quark-antiquark-pairs $\gamma^\star \to q\bar{q} \to \gamma^\star$, is possible by measuring the cross section of electron positron annihilation into hadrons $e^+e^- \to \gamma^* \to q\bar{q} \to hadrons$ applying the optical theorem. It is of great importance for the interpretation of the precision measurement of the anomalous magnetic moment of the muon a_μ in *Brookhaven (E821)* [71–74] and for the determination of the value of the running fine structure constant at the Z^o resonance $\alpha(m_Z^2)$, contributing to precision tests of the *Standard model* of particle physics, see for details e. g. *Jegerlehner* [75], also *Davier* and *Marciano* [76], or *Teubner et al.* [77–79]. The hadronic contribution to a_μ below about 2 GeV is dominated by the 2π final state, which contributes about 70 % due to the dominance of the $\rho-$resonance. Other major contributions come from the three- and four-pion final states. These hadronic final states constitute at present the largest error to the *Standard model* value of a_μ and $\alpha(m_Z^2)$ and can be determined only experimentally because calculations within perturbative *QCD* are unrealistic, calculations on the lattice are not yet available with necessary accuracy, and calculations in the framework of chiral perturbation theory are restricted to values close to the reaction thresholds. At energies above about 2 to 2.5 GeV perturbative *QCD* calculations start to become possible and reliable, see for Refs. [80,81], also [82].

The *Novosibirsk* groups $CMD-2$ [5,83–91] and SND [92–97] measured hadronic cross sections below 1.4 GeV by changing the collider energy (*energy scan*, see preceding Section 3). The *Initial State Radiation* method used by *KLOE* represents an alternative, independent and complementary way to determine hadronic cross sections with different systematic errors. *KLOE* has determined the cross section for the reaction $e^+e^- \to \pi^+\pi^-$ in the energy region between 0.63 and 0.958 GeV by measuring the reaction $e^+e^- \to \pi^+\pi^-\gamma$ and applying a radiator function based on *PHOKHARA*. It obtained for the hadronic contribution to the anomalous magnetic moment of the muon due to the 2π final state $a_\mu^{\pi\pi} = (356.7 \pm 3.1_{stat+syst}) \cdot 10^{-10}$ [68]. This value is in good agreement with those from *SND* [97] and *CMD-2* [91]: $a_\mu^{\pi\pi} = (361.0 \pm 5.1_{stat+syst}) \cdot 10^{-10}$ and $a_\mu^{\pi\pi} = (361.5 \pm 3.4_{stat+syst}) \cdot 10^{-10}$, respectively, leading to an evaluation of a_μ [75–79,98] which differs by about 3 standard deviations from the BNL experiment [73]. A different evaluation using τ -decays into 2 pions results in a reduced discrepancy [76,98]. The difference between e^+e^-- and $\tau-$based analyses is at present not understood. But one has to be aware that the evaluation with τ data needs more theoretical input.

Soon after the application of *EVA-PHOKHARA* to *KLOE* [46] the *BABAR* collaboration also started the measurement of hadronic cross sections exploiting *ISR* [99] and using *PHOKHARA* (Section 4.4.2). In recent years a plethora of final states has been studied, starting with the reaction $e^+e^- \to J/\psi\,\gamma \to \mu^+\mu^-\,\gamma$ [100]. While detecting a hard photon the upper energy for the hadron cross sections is limited to roughly 4.5 GeV. Final states with 3, 4, 5, 6 charged and neutral pions , 2 pions and 2 kaons, 4 kaons, 4 pions and 2 kaons, with a ϕ and a $f_o(980)$, J/ψ and 2 pions or 2 kaons, pions and η, kaons and η, but also baryonic final states with protons and antiprotons, Λ^o and $\bar{\Lambda}^o$, Λ^o and $\bar{\Sigma}^o$, Σ^o and $\bar{\Sigma}^o$, $D\bar{D}$, $D\bar{D}^*$, and $D^*\bar{D}^*$ mesons, etc. have been investigated [101–113]. In preparation are final states with 2 pions [114] and 2 kaons. Particularly important final states are those with 4 pions (including $\omega\pi^o$) which contribute significantly to the muon anomalous magnetic moment and which were poorly known before the *ISR* measurements. In many of these channels additional insights into isospin symmetry breaking are expected from the comparison between e^+e^- annihilation and τ decays.

More recently also *Belle* joined the *ISR* programme with emphasis on final states containing mesons with hidden and open charm: J/ψ and $\psi(2S)$, D and $\bar{D}$, ${\Lambda_c}^+{\Lambda_c}^-$ [115–122] (Section 4.4.3).

A major surprise in recent years was the opening of a totally new field of hadron spectroscopy applying *ISR*. Several new relatively narrow highly excited states with $J^{PC} = 1^{--}$, the quantum numbers of the photon, have been discovered (preliminarily denoted as *X, Y, Z*) at the B-factories *PEP-II* and *KEKB* with the detectors *BABAR* and *Belle*, respectively. The first of them was found by *BABAR* in the reaction $e^+e^- \to Y(4260)\,\gamma \to J/\psi\,\pi^+\pi^-\gamma$ [123,124], a state around 4260 MeV with a width of 90 MeV, later confirmed by *Belle* via *ISR* [125, 116,126] and by *CLEO* in an direct energy scan [127] and a radiative return [128] . Another state was detected at 2175 MeV by *BABAR* in the reaction $e^+e^- \to Y(2175)\,\gamma \to \phi f_o(980)\gamma$ [105]. *Belle* found new states at 4050, 4360, 4660 MeV in the reactions $e^+e^- \to Y\gamma \to J/\psi\pi^+\pi^-\gamma$ and $e^+e^- \to Y\gamma \to \psi(2S)\pi^+\pi^-\gamma$ [127,117,116]. The structure of basically all of these new states (if they will survive) is unknown so far. Four-quark states, e. g. a $[cs][\bar{c}\bar{s}]$ state for $Y(4260)$, a $[ss][\bar{s}\bar{s}]$ state for $Y(2175)$, hybrid and molecular structures are discussed, see also [129].

Detailed analyses allow, in addition, also the identification of intermediate states and consequently a study of reaction mechanisms. For instance, in the case of the final state with 2 charged and 2 neutral pions ($e^+e^- \to \pi^+\pi^-\pi^o\pi^o\gamma$) the dominating intermediate states are $\omega\pi^o$ and $a_1(1260)\pi$, while $\rho^+\rho^-$ and $\rho^o f_o(980)$ contribute significantly less.

Many more highly excited states with quantum numbers, different from those of the photon, have been found in decay chains of the primarily produced heavy mesons at the *B*-factories *PEP-II* and *KEKB*. These analyses without *ISR* have clearly been triggered and encouraged by the unexpected discovery of highly excited states with $J^{PC} = 1^{--}$ found with *ISR*.

Also baryonic final states with protons and antiprotons, Λ^o and $\bar{\Lambda}^o$, Λ^o and $\bar{\Sigma}^o$, Σ^o and $\bar{\Sigma}^o$ have been investigated using *ISR*. The effective proton form factor (see

Section 4.4.2) shows a strong increase down to the $p\bar{p}$ threshold and nontrivial structures at invariant $p\bar{p}$ masses of 2.25 and 3.0 GeV, so far unexplained [103,130–133]. Furthermore, it should be possible to disentangle electric and magnetic form factors and thus shed light on discrepancies between different measurements of these quantities in the spacelike region [134].

Prospects for the *Radiative Return* at the *Novosibirsk* collider *VEPP2000* and *BEPCII* are discussed in Sections 4.4.4 and 4.4.5.

4.2 Radiative return: A theoretical overview

4.2.1 Radiative return at leading order

We consider the e^+e^- annihilation process

$$e^+(p_1) + e^-(p_2) \to \text{hadrons} + \gamma(k_1) \ , \tag{1}$$

where the real photon is emitted either from the initial (Fig. 2a) or the final state (Fig. 2b). The former process is denoted initial state radiation (ISR), while the latter is called final state radiation (FSR).

The differential rate for the ISR process can be cast into the product of a leptonic $L^{\mu\nu}$ and a hadronic $H^{\mu\nu}$ tensor and the corresponding factorized phase space

$$d\sigma_{\mathrm{ISR}} = \frac{1}{2s} L^{\mu\nu}_{\mathrm{ISR}} H_{\mu\nu} \\ \times d\Phi_2(p_1,p_2;Q,k_1) d\Phi_n(Q;q_1,\cdot,q_n)\frac{dQ^2}{2\pi} \ , \tag{2}$$

where $d\Phi_n(Q;q_1,\cdot,q_n)$ denotes the hadronic n-body phase-space with all the statistical factors coming from the hadronic final state included, $Q = \sum q_i$ and $s = (p_1+p_2)^2$.

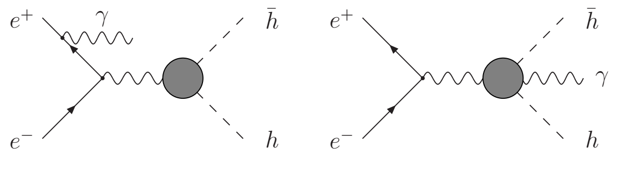

(a) (b)

Fig. 2. Leading order contributions to the reaction $e^+e^- \to h\,\bar{h}+\gamma$ from ISR (a) and FSR (b). Final state particles are pions or muons, or any other multihadron state. The blob represents the hadronic form factor.

For an arbitrary hadronic final state, the matrix element for the diagrams in Fig. 2a is given by

$$\mathcal{A}^{(0)}_{\mathrm{ISR}} = M^{(0)}_{\mathrm{ISR}} \cdot J^{(0)} = \\ = -\frac{e^2}{Q^2}\bar{v}(p_1)\left(\frac{\not\epsilon^*(k_1)[\not k_1 - \not p_1 + m_e]\gamma^\mu}{2k_1\cdot p_1} \right. \\ \left. + \frac{\gamma^\mu[\not p_2 - \not k_1 + m_e]\not\epsilon^*(k_1)}{2k_1\cdot p_2}\right) u(p_2)\ J^{(0)}_\mu \ , \tag{3}$$

where J_μ is the hadronic current. The superscript (0) indicates that the scattering amplitude is evaluated at tree-level. Summing over the polarizations of the final real photon, averaging over the polarizations of the initial e^+e^- state, and using current conservation, $Q\cdot J^{(0)} = 0$, the leptonic tensor

$$L^{(0),\mu\nu}_{\mathrm{ISR}} = \overline{M^{(0),\,\mu}_{\mathrm{ISR}}(M^{(0),\,\nu}_{\mathrm{ISR}})^\dagger} \ ,$$

can be written in the following form:

$$L^{(0),\,\mu\nu}_{\mathrm{ISR}} = \frac{(4\pi\alpha)^2}{Q^4}\left[\left(\frac{2m^2q^2(1-q^2)^2}{y_1^2y_2^2} - \frac{2q^2+y_1^2+y_2^2}{y_1y_2}\right)g^{\mu\nu} \right. \\ + \left(\frac{8m^2}{y_2^2} - \frac{4q^2}{y_1y_2}\right)\frac{p_1^\mu p_1^\nu}{s} + \left(\frac{8m^2}{y_1^2} - \frac{4q^2}{y_1y_2}\right)\frac{p_2^\mu p_2^\nu}{s} \\ \left. - \left(\frac{8m^2}{y_1y_2}\right)\frac{p_1^\mu p_2^\nu + p_1^\nu p_2^\mu}{s}\right] \ , \tag{4}$$

with

$$y_i = \frac{2k_1\cdot p_i}{s} \ , \qquad m^2 = \frac{m_e^2}{s} \ , \qquad q^2 = \frac{Q^2}{s} \ . \tag{5}$$

The leptonic tensor is symmetric under the exchange of the electron and the positron momenta. Expressing the bilinear products y_i by the photon emission angle in the c.m. frame

$$y_{1,2} = \frac{1-q^2}{2}(1\mp\beta\cos\theta) \ , \qquad \beta = \sqrt{1-4m^2} \ ,$$

and rewriting the two-body phase space

$$d\Phi_2(p_1,p_2;Q,k_1) = \frac{1-q^2}{32\pi^2}d\Omega \ , \tag{6}$$

it is evident that expression (4) contains several singularities: soft singularities for $q^2 \to 1$ and collinear singularities for $\cos\theta \to \pm 1$. The former are avoided by requiring a minimal photon energy. The later are regulated by the electron mass. For $s \gg m_e^2$, the expression (4) can be nevertheless safely taken in the limit $m_e \to 0$ if the emitted real photon lies far from the collinear region. In general, however, one encounters spurious singularities in the phase space integrations if powers of $m^2 = m_e^2/s$ are prematurely neglected.

Physics of the hadronic system, whose description is model dependent, enters through the hadronic tensor

$$H_{\mu\nu} = J^{(0)}_\mu (J^{(0)}_\nu)^\dagger \ , \tag{7}$$

where the hadronic current has to be parameterized through form factors. For two charged pions in the final state, the current

$$J^{(0),\,\mu}_{\pi^+\pi^-} = ieF_{2\pi}(Q^2)\ (q_1-q_2)^\mu \ , \tag{8}$$

where q_1 and q_2 are the momenta of the π^+ and π^-, respectively, is determined by only one function, the pion form factor $F_{2\pi}$. The current for the $\mu^+\mu^-$ final state is defined obviously by QED:

$$J^{(0),\,\mu}_{\mu^+\mu^-} = ie\,\bar{u}(q_2)\gamma^\mu v(q_1) \ . \tag{9}$$

Integrating the hadronic tensor over the hadronic phase space, one gets

$$\int H^{\mu\nu} d\Phi_n(Q; q_1, \cdot, q_n) = \frac{e^2}{6\pi}(Q^\mu Q^\nu - g^{\mu\nu} Q^2) R(Q^2) \ , \tag{10}$$

where $R(Q^2) = \sigma(e^+e^- \to \text{hadrons})/\sigma_0(e^+e^- \to \mu^+\mu^-)$, with

$$\sigma_0(e^+e^- \to \mu^+\mu^-) = \frac{4\pi\,\alpha^2}{3Q^2} \tag{11}$$

the tree-level muonic cross section in the limit $Q^2 \gg 4m_\mu^2$. After the additional integration over the photon angles, the differential distribution

$$Q^2 \frac{d\sigma_{\rm ISR}}{dQ^2} = \frac{4\alpha^3}{3s} R(Q^2) \left\{ \frac{s^2 + Q^4}{s(s-Q^2)} (L-1) \right\} \ , \tag{12}$$

with $L = \log(s/m_e^2)$ is obtained. If instead the photon polar angle is restricted to be in the range $\theta_{\rm min} < \theta < \pi - \theta_{\rm min}$, this differential distribution is given by

$$Q^2 \frac{d\sigma_{\rm ISR}}{dQ^2} = \frac{4\alpha^3}{3s} R(Q^2) \left\{ \frac{s^2 + Q^4}{s(s-Q^2)} \log \frac{1+\cos\theta_{\rm min}}{1-\cos\theta_{\rm min}} - \frac{s-Q^2}{s}\cos\theta_{\rm min} \right\} \ . \tag{13}$$

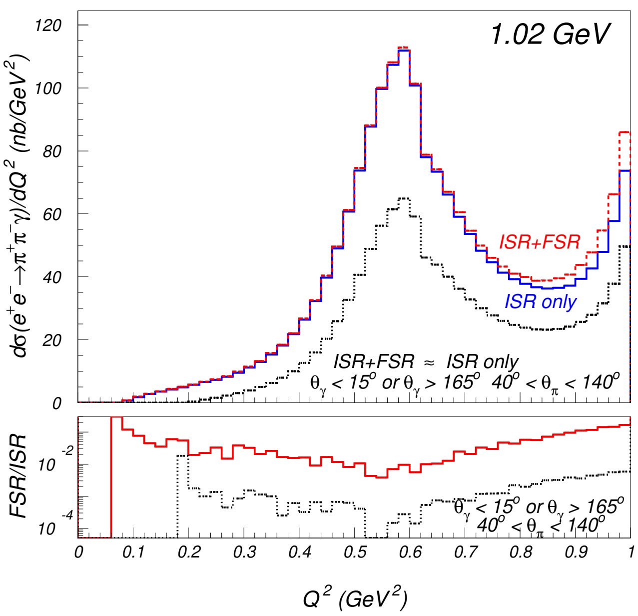

Fig. 3. The suppression of the FSR contributions to the cross section by a suitable choice of angular cuts. Results from the PHOKHARA generator. No cuts (upper curves) and suitable cuts applied (lower curves).

In the later case, the electron mass can be taken equal to zero before integration, since the collinear region is excluded by the angular cut. The contribution of the two-pion exclusive channel can be calculated from Eq.(12) and Eq.(13) with

$$R_{\pi^+\pi^-}(Q^2) = \frac{1}{4}\left(1 - \frac{4m_\pi^2}{Q^2}\right)^{3/2} |F_{2\pi}(Q^2)|^2 \ , \tag{14}$$

and the corresponding muonic contribution with

$$R_{\mu^+\mu^-}(Q^2) = \sqrt{1 - \frac{4m_\mu^2}{Q^2}} \left(1 + \frac{2m_\mu^2}{Q^2}\right) \ . \tag{15}$$

A potential complication for the measurement of the hadronic cross section from the radiative return may arise from the interplay between photons from ISR and FSR [23]. Their relative strength is strongly dependent on the photon angle relative to the beam and to the direction of the final state particles, the c.m. energy of the reaction and the invariant mass of the hadronic system. While ISR is independent of the hadronic final state, FSR is not. Moreover, it cannot be predicted from first principles and thus has to be modeled.

The amplitude for FSR (Fig. 2b) factorizes as well as

$$\mathcal{A}_{\rm FSR}^{(0)} = M^{(0)} \cdot J_{\rm FSR}^{(0)} \ , \tag{16}$$

where

$$M_\mu^{(0)} = \frac{e}{s}\,\bar{v}(p_1)\gamma_\mu u(p_2) \ . \tag{17}$$

Assuming that pions are point-like, the FSR current for two pions in scalar QED (sQED) reads

$$J_{\rm FSR}^{(0),\,\mu} = -i\,e^2\,F_{2\pi}(s) \times \left[-2g^{\mu\sigma} + (q_1 + k_1 - q_2)^\mu \frac{(2q_1+k_1)^\sigma}{2k_1\cdot q_1} - (q_1 - k_1 - q_2)^\mu \frac{(2q_2+k_1)^\sigma}{2k_1\cdot q_2} \right] \epsilon_\sigma^*(k_1) \ . \tag{18}$$

Due to momentum conservation, $p_1 + p_2 = q_1 + q_2 + k_1$, and current conservation, this expression can be simplified further to

$$J_{\rm FSR}^{(0),\,\mu} = 2i\,e^2\,F_{2\pi}(s) \left[g^{\mu\sigma} + \frac{q_2^\mu\, q_1^\sigma}{k_1\cdot q_1} + \frac{q_1^\mu\, q_2^\sigma}{k_1\cdot q_2} \right] \epsilon_\sigma^*(k_1) \ . \tag{19}$$

This is the basic model adopted in EVA [23] and in PHOKHARA [25–32,35,135] to simulate FSR off charged pions. The corresponding FSR current for muons is given by QED.

The fully differential cross section describing photon emission at leading order can be split into three pieces

$$d\sigma^{(0)} = d\sigma_{\rm ISR}^{(0)} + d\sigma_{\rm FSR}^{(0)} + d\sigma_{\rm INT}^{(0)} \ , \tag{20}$$

which originate from the squared ISR and FSR amplitudes respectively, plus the interference term. The ISR–FSR interference, is odd under charge conjugation,

$$d\sigma_{\rm INT}^{(0)}(q_1, q_2) = -d\sigma_{\rm INT}^{(0)}(q_2, q_1) \ , \tag{21}$$

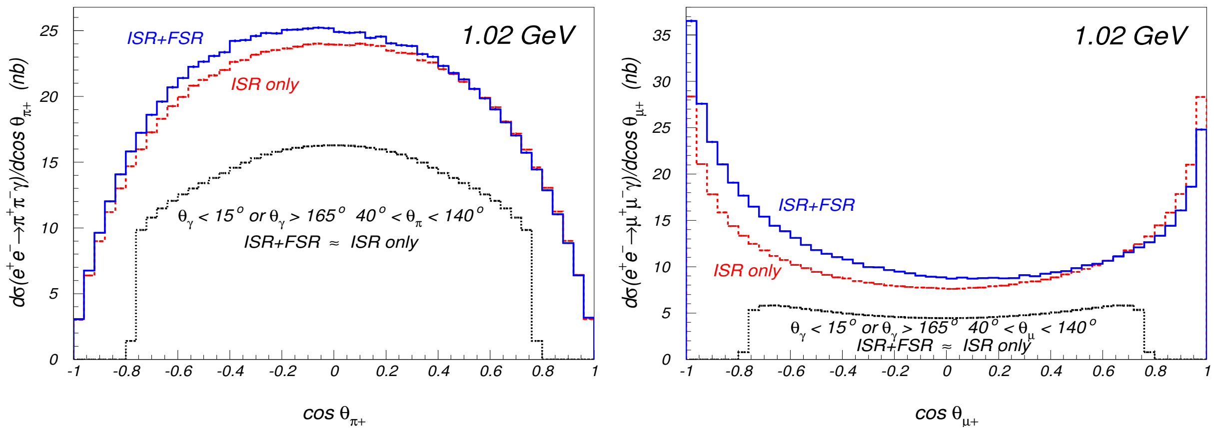

Fig. 4. Angular distributions of π^+ and μ^+ at $\sqrt{s} = 1.02$ GeV with and without FSR for different angular cuts.

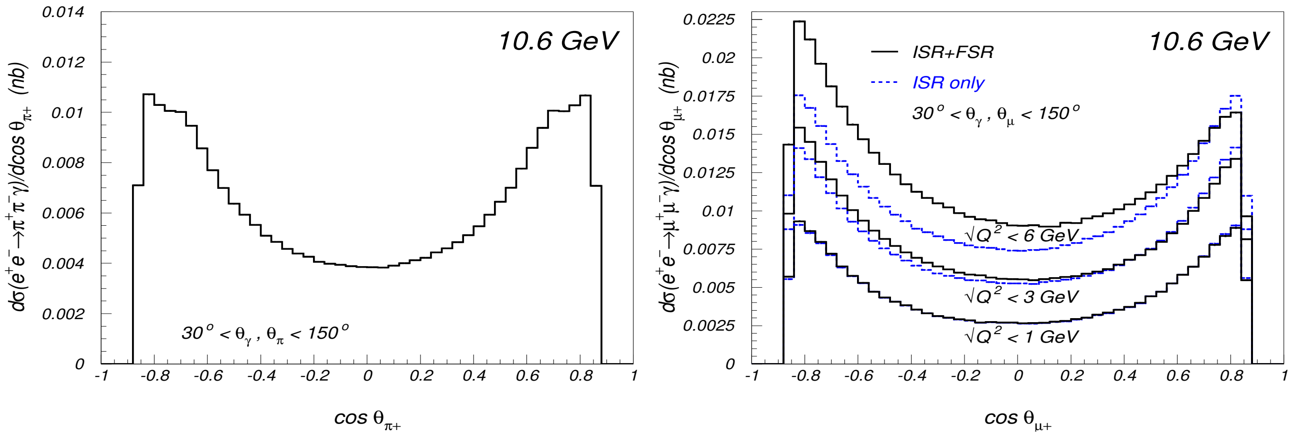

Fig. 5. At $\sqrt{s}$=10.6 GeV, angular distribution of π^+ (ISR $\simeq$ FSR+ISR) and of μ^+ for various Q^2 cuts.

and its contribution vanishes after angular integration. It gives rise, however, to a relatively large charge asymmetry and, correspondingly, to a forward–backward asymmetry

$$A(\theta) = \frac{N_h(\theta) - N_h(\pi - \theta)}{N_h(\theta) + N_h(\pi - \theta)} \,. \qquad (22)$$

The asymmetry can be used for calibration of the FSR amplitude, and fits to the angular distribution $A(\theta)$ can test details of its model dependence [23].

The second option to disentangle ISR from FSR exploits the markedly different angular distribution of the photon from the two processes. This observation is completely general and does not rely on any model like sQED for FSR. FSR is dominated by photons collinear to the final state particles, while ISR is dominated by photons collinear to the beam direction. This suggests that we should consider only events with photons well separated from the charged final state particles and preferentially close to the beam [23,27,28].

This is illustrated in Fig. 3, which has been generated running PHOKHARA at leading order (LO). After introducing suitable angular cuts the contamination of events

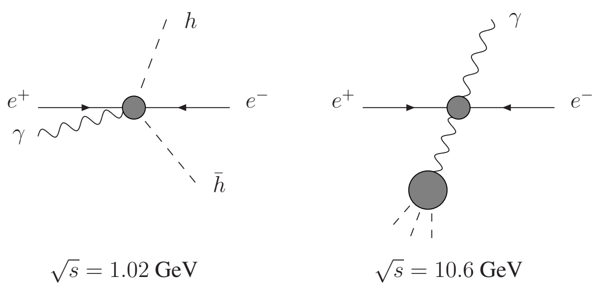

Fig. 6. Typical kinematic configuration of the radiative return at low and high energies.

with FSR is easily reduced to less than a few per mille. The price to pay, however, is a suppression of the threshold region too. To have access to that region photons at large angles need to be tagged, and a better control of FSR is required. In Fig. 4 the angular distribution of π^+ and μ^+ at DAPHNE energies, $\sqrt{s} = 1.02$ GeV, are shown for different angular cuts. The angles are defined with respect to the incoming positron. If no angular cut is applied, the angular distribution in both cases is highly asymmetric as a consequence of the ISR–FSR interference contribution. If cuts suitable to suppress FSR, and therefore the ISR–FSR interference, are applied, the distributions become symmetric.

Two complementary analyses are therefore possible (for details see Section 4.4.1): The *small photon angle* analysis, where the photon is untagged and FSR can be suppressed below some reasonable limit. This analysis is suitable for intermediate values of the invariant mass of the hadronic system. And the *large photon angle* analysis, giving access to the threshold region, where FSR is more pronounced and the charge asymmetry is a useful tool to probe its model dependence.

These considerations apply, however, to low beam energies, around 1 GeV. At high energies, e.g. at B-factories, very hard tagged photons are needed to access the region with low hadronic invariant masses and the hadronic system is mainly produced back to back to the hard photon. The suppression of FSR is naturally accomplished and no special angular cuts are needed. This kinematical situation is illustrated in Fig. 6. The suppression of FSR contributions to $\pi^+\pi^-\gamma$ events is also a consequence of the rapid decrease of the form factor above 1 GeV. The relative size of FSR is of the order of a few per mil (see Fig. 5). For $\mu^+\mu^-$ in the final state, the amount of FSR depends on the invariant mass of the muons. For $\sqrt{Q^2} < 1$ GeV FSR is still tiny, and becomes more relevant for larger values of Q^2 (see Fig. 5).

4.2.2 Structure functions

The original and default version of EVA [23], simulating the process $e^+e^- \to \pi^+\pi^-\gamma$ at LO, allowed for additional initial state radiation of soft and collinear photons by the structure function (SF) method [136,40].

In the leading logarithmic approximation (LL), the multiple emission of collinear photons off an electron is described by the convolution integral

$$\sigma(e^-X \to Y + n\gamma) = \int_0^1 dx\, f_e(x,Q^2)\, \sigma(e^-X \to Y) \ , \tag{23}$$

where $f_e(x,Q^2)$ is the probability distribution of the electron with longitudinal momentum fraction x, and Q is the transverse momentum of the collinear photons. The function $f_e(x,Q^2)$ fulfills the evolution equation

$$\frac{d}{d\log Q} f_e(x,Q^2) = \int_x^1 \frac{dz}{z} \frac{\alpha}{\pi}\left(\frac{1+z^2}{(1-z)_+} + \frac{3}{2}\delta(1-z)\right) f_e(\frac{x}{z},Q^2) \ , \tag{24}$$

with initial conditions

$$f_e(x,Q^2)\big|_{Q^2=m_e^2} = \delta(1-x) \ , \tag{25}$$

and the + prescription defined as

$$\int_0^1 dx\, \frac{f(x)}{(1-x)_+} = \int_0^1 dx\, \frac{f(x)-f(1)}{(1-x)} \ . \tag{26}$$

The analytic solution to Eq.(24) provided in Ref. [136, 40], allows to resum soft photons to all orders in perturbation theory, accounting for large logarithms of collinear origin, $L = \log(s/m_e^2)$, up to two loops. The resummed cross section

$$\sigma_{\rm SF} = \int_0^1 dx_1 \int_0^1 dx_2\, D(x_1)\, D(x_2)\, \sigma_{e^+e^-\to{\rm had.}+\gamma}(x_1 x_2 s) \ , \tag{27}$$

is thus obtained by convoluting the Born cross section of the hard photon emission process $e^+e^- \to$ hadrons $+ \gamma$ with the SF distribution [136,40]

$$\begin{aligned} D(x) = {} & [1+\delta_N]^{1/2}\, \frac{\beta_e}{2}(1-x)^{\frac{\beta_e}{2}-1} \\ & \times\Bigg\{\frac{1}{2}(1+x^2) + \frac{1}{2}\frac{(1-x)^2}{L-1} \\ & + \frac{\beta_e}{8}\left(-\frac{1}{2}(1+3x^2)\log x - (1-x)^2\right)\Bigg\} \ , \end{aligned} \tag{28}$$

with

$$\beta_e = 2\,\frac{\alpha}{\pi}\,(L-1) \ , \tag{29}$$

and

$$\begin{aligned} \delta_N = {} & \frac{\alpha}{\pi}\left(\frac{3}{2}L + \frac{\pi^2}{3} - 2\right) \\ & + \beta_e^2\frac{\pi^2}{8} + \left(\frac{\alpha}{\pi}\right)^2\left(\frac{11}{8} - \frac{2\pi^2}{3}\right) L^2 \ . \end{aligned} \tag{30}$$

In the SF approach, the additional emission of collinear photons reduces the effective c.m. energy of the collision to $\sqrt{x_1 x_2 s}$. Momentum conservation is not accomplished because the extra radiation is integrated out. In order to reduce the kinematic distortion of the events, a minimal invariant mass of the observed particles, hadrons plus the tagged photon, was required in [23], introducing then a cut dependence. The SF predictions are, thus, not accurate enough for a high precision measurement of the hadronic cross section from the radiative return. A next-to-leading order (NLO) calculation is in order. The NLO prediction contains the large logarithms $L = \log(s/m_e^2)$ at order α^3 and additional subleading terms, which are not taken into account within the SF method. Furthermore, it allows for a better control of the kinematical configurations because of momentum conservation. A comparison between SF and NLO predictions can be found in [27].

4.2.3 Radiative return at NLO

At NLO, the e^+e^- annihilation process in Eq.(1) receives contributions from one-loop corrections and from the emission of a second real photon (see Fig. 7). After renormalization, the one-loop matrix elements still contain infrared

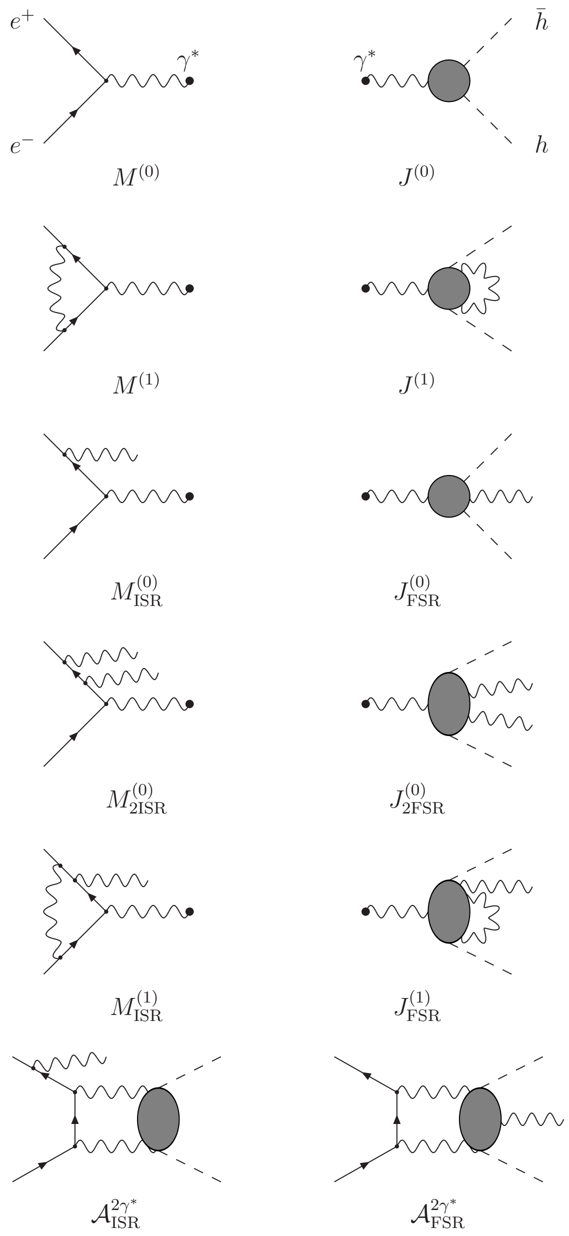

Fig. 7. Typical subamplitudes describing virtual and real corrections to the reaction $e^+e^- \to h\bar{h} + \gamma(\gamma)$, where $h = \pi^-$, μ^-. The superscripts (0) and (1) denote tree-level and one-loop quantities, respectively. ISR and FSR indicate that real photons are emitted from the initial or final state. The last two diagrams, with exchange of two virtual photons are non-factorizable. Permutations are omitted.

divergences. These are canceled by adding to the one-loop corrections the two-photon contributions. There are several well established methods to perform this cancellation. The slicing method, where amplitudes are evaluated in dimensional regularization and the two photon contribution is integrated analytically in phase space for one of the photon energies up to an energy cutoff $E_\gamma < w\sqrt{s}$ far below $\sqrt{s}$, was used in [25,26] to calculate the NLO corrections to ISR. The sum of the virtual and soft contributions is finite although depends on the soft photon cutoff. The contribution from the emission of the second photon with energy $E_\gamma > w\sqrt{s}$, which is evaluated numerically, completes the calculation and cancels this dependence.

The size and sign of the NLO corrections do depend on the particular choice of the experimental cuts. Hence, only using a Monte Carlo event generator one can realistically compare theoretical predictions with experiment. This is the main motivation behind PHOKHARA [25–32,35,135].

The full set of scattering amplitudes at tree-level and one-loop can be constructed from the subamplitudes depicted in Fig. 7. The one-loop amplitude with emission of a single photon is given by

$$\begin{aligned}\mathcal{A}^{(1)}_{1\gamma} &= \mathcal{A}^{(1)}_{\mathrm{ISR}} + \mathcal{A}^{(1)}_{\mathrm{FSR}} \\ &\quad + M^{(1)} \cdot J^{(0)}_{\mathrm{FSR}} + M^{(0)}_{\mathrm{ISR}} \cdot J^{(1)} \\ &\quad + \mathcal{A}^{2\gamma^*}_{\mathrm{ISR}} + \mathcal{A}^{2\gamma^*}_{\mathrm{FSR}} \ , \end{aligned} \tag{31}$$

where

$$\mathcal{A}^{(1)}_{\mathrm{ISR}} = M^{(1)}_{\mathrm{ISR}} \cdot J^{(0)} \ , \qquad \mathcal{A}^{(1)}_{\mathrm{FSR}} = M^{(0)} \cdot J^{(1)}_{\mathrm{FSR}} \ , \tag{32}$$

while the amplitude with emission of two real photons reads

$$\begin{aligned}\mathcal{A}^{(0)}_{2\gamma} &= \mathcal{A}^{(0)}_{\mathrm{2ISR}} + \mathcal{A}^{(0)}_{\mathrm{2FSR}} \\ &\quad + \left(M^{(0)}_{\mathrm{ISR}}(k_1) \cdot J^{(0)}_{\mathrm{FSR}}(k_2) + (k_1 \leftrightarrow k_2) \right) \ , \end{aligned} \tag{33}$$

where

$$\mathcal{A}^{(0)}_{\mathrm{2ISR}} = M^{(0)}_{\mathrm{2ISR}} \cdot J^{(0)} \ , \qquad \mathcal{A}^{(0)}_{\mathrm{2FSR}} = M^{(0)} \cdot J^{(0)}_{\mathrm{2FSR}} \ . \tag{34}$$

PHOKHARA includes the full LO amplitudes and the most relevant C-even NLO contributions:

$$d\sigma = d\sigma^{(0)} + d\sigma^{(1)}_{\mathrm{ISR}} + d\sigma^{(1)}_{\mathrm{IFS}} \ , \tag{35}$$

where $d\sigma^{(0)}$ is the LO differential cross section (Eq.(20)),

$$\begin{aligned} d\sigma^{(1)}_{\mathrm{ISR}} &= \frac{1}{2s} \left[2\mathrm{Re} \left\{ \mathcal{A}^{(1)}_{\mathrm{ISR}} \left(\mathcal{A}^{(0)}_{\mathrm{ISR}} \right)^\dagger \right\} d\Phi_3(p_1,p_2;q_1,q_2,k_1) \right. \\ &\quad \left. + \left| \mathcal{A}^{(0)}_{\mathrm{2ISR}} \right|^2 d\Phi_4(p_1,p_2;q_1,q_2,k_1,k_2) \right] \ , \end{aligned} \tag{36}$$

is the second order radiative corrections to ISR, and

$$\begin{aligned} d\sigma^{(1)}_{\mathrm{IFS}} &= \frac{1}{2s} \left[2\mathrm{Re} \left\{ M^{(0)}_{\mathrm{ISR}} \cdot J^{(1)} \left(\mathcal{A}^{(0)}_{\mathrm{ISR}} \right)^\dagger \right. \right. \\ &\quad \left. + M^{(1)} \cdot J^{(0)}_{\mathrm{FSR}} \left(\mathcal{A}^{(0)}_{\mathrm{FSR}} \right)^\dagger \right\} d\Phi_3(p_1,p_2;q_1,q_2,k_1) \\ &\quad + \left(\left| M^{(0)}_{\mathrm{ISR}}(k_1) \cdot J^{(0)}_{\mathrm{FSR}}(k_2) \right|^2 + (k_1 \leftrightarrow k_2) \right) \\ &\quad \left. \times d\Phi_4(p_1,p_2;q_1,q_2,k_1,k_2) \right] \ , \end{aligned} \tag{37}$$

is the contribution of events with simultaneous emission of one photon from the initial state and another one from the final state, together with ISR amplitudes with final state one-loop vertex corrections, and FSR amplitudes with initial state one-loop vertex corrections. We denote these corrections as IFS.

Vacuum polarization corrections are included in the hadronic currents multiplicatively:

$$\begin{aligned} J^{(i)} &\to C_{\rm VP}(Q^2)\, J^{(i)} \ , \\ J^{(i)}_{\rm FSR}(k_j) &\to C_{\rm VP}((Q+k_j)^2)\, J^{(i)}_{\rm FSR}(k_j) \ , \\ J^{(0)}_{\rm 2FSR} &\to C_{\rm VP}(s)\, J^{(0)}_{\rm 2FSR} \ . \end{aligned} \tag{38}$$

The virtual photon propagator is included by definition in the leptonic subamplitudes $M^{(i)}$ and $M^{(i)}_{\rm ISR}$, and $M^{(0)}_{\rm 2ISR}$:

$$\begin{aligned} M^{(i)} &\sim \frac{1}{s} \ , \\ M^{(i)}_{\rm ISR}(k_j) &\sim \frac{1}{(p_1+p_2+k_j)^2} \\ M^{(0)}_{\rm 2ISR} &\sim \frac{1}{Q^2} \ . \end{aligned} \tag{39}$$

Neither diagrams where two photons are emitted from the final state nor final-state vertex corrections with associated real radiation from the final state are included. These constitute radiative corrections to FSR and will give non-negligible contributions only for those cases, where at least one photon is collinear with one of the final state particles. Box diagrams with associated real radiation from the initial- or the final-state leptons, as well as pentagon diagrams, are also neglected. As long as one considers charge symmetric observables only, their contribution is neither divergent in the soft nor the collinear limit and is thus of order α/π without any enhancement factor. One should stress that PHOKHARA includes only C-even gauge invariant sets of diagrams at NLO. The missing contributions are either small, or do not contribute for charge symmetric cuts. Their implementation is, however, underway.

The calculation of the NLO corrections to ISR, $d\sigma^{(1)}_{\rm ISR}$, is independent of the final state. These corrections are included by default for all the final state channels implemented in PHOKHARA, and can be easily added for any other new channel, with the sole substitution of the tree-level final state current. The radiative corrections of the IFS process depend on the final state. The latest version of PHOKHARA (version 6.0 [35]) includes these corrections for two charged pions, kaons and muons.

Virtual and soft corrections to ISR

The virtual and soft QED corrections to ISR in e^+e^- annihilation were originally implemented in PHOKHARA through the leptonic tensor. For future applications, however, it will be more convenient to implement those corrections directly at the amplitude level (in preparation). In terms of subamplitudes, the leptonic tensor is given by

$$\begin{aligned} L^{\mu\nu}_{\rm ISR} &= L^{(0),\mu\nu}_{\rm ISR} + M^{(1),\,\mu}_{\rm ISR}\left(M^{(0),\,\nu}_{\rm ISR}\right)^\dagger + M^{(0),\,\mu}_{\rm ISR}\left(M^{(1),\,\nu}_{\rm ISR}\right)^\dagger \\ &+ \frac{1}{2(2\pi)^{d-1}}\int_0^{w\sqrt{s}} E^{d-3}\, dE\, d\Omega\, M^{(0),\,\mu}_{\rm 2ISR}\left(M^{(0),\,\nu}_{\rm 2ISR}\right)^\dagger \ , \end{aligned} \tag{40}$$

where E and Ω are the energy and the solid angle of the soft photon, respectively, and $d = 4 - 2\epsilon$ is the number of dimensions in dimensional regularization. The leptonic tensor has the following general form:

$$\begin{aligned} L^{\mu\nu}_{\rm ISR} = \frac{(4\pi\alpha)^2}{Q^4}\Bigg[& a_{00}\, g^{\mu\nu} + a_{11}\, \frac{p_1^\mu p_1^\nu}{s} + a_{22}\, \frac{p_2^\mu p_2^\nu}{s} \\ & + a_{12}\, \frac{p_1^\mu p_2^\nu + p_2^\mu p_1^\nu}{s} + i\pi\, a_{-1}\, \frac{p_1^\mu p_2^\nu - p_2^\mu p_1^\nu}{s} \Bigg] \ , \end{aligned} \tag{41}$$

where the scalar coefficients a_{ij} and a_{-1} allow the following expansion:

$$a_{ij} = a^{(0)}_{ij} + \frac{\alpha}{\pi}\, a^{(1)}_{ij} \ , \qquad a_{-1} = \frac{\alpha}{\pi}\, a^{(1)}_{-1} \ . \tag{42}$$

The imaginary antisymmetric piece, which is proportional to a_{-1}, appears for the first time at second order, and is particularly relevant for those cases where the hadronic current receives contributions from different amplitudes with non-trivial relative phases. This is possible, e.g. for final states with three or more mesons or for $p\bar{p}$ production.

The LO coefficients $a^{(0)}_{ij}$ can be read directly from Eq.(4)

$$\begin{aligned} a^{(0)}_{00} &= \frac{2m^2q^2(1-q^2)^2}{y_1^2y_2^2} - \frac{2q^2+y_1^2+y_2^2}{y_1y_2} \ , \\ a^{(0)}_{11} &= \frac{8m^2}{y_2^2} - \frac{4q^2}{y_1y_2} \ , \qquad a^{(0)}_{22} = a^{(0)}_{11}(y_1 \leftrightarrow y_2) \ , \\ a^{(0)}_{12} &= -\frac{8m^2}{y_1y_2} \ . \end{aligned} \tag{43}$$

The NLO coefficients $a^{(1)}_{ij}$ and $a^{(1)}_{-1}$ are obtained by combining the one-loop and the soft contributions. It is convenient to split the coefficients $a^{(1)}_{ij}$ into a part that contributes at large photon angles and a part proportional to m_e^2 and m_e^4 which is relevant only in the collinear regions. These coefficients are denoted by $a^{(1,0)}_{ij}$ and $a^{(1,m)}_{ij}$ respectively:

$$\begin{aligned} a^{(1)}_{ij} = a^{(0)}_{ij}\Bigg[& -\log(4w^2)[1+\log(m^2)] \\ & - \frac{3}{2}\log(\frac{m^2}{q^2}) - 2 + \frac{\pi^2}{3}\Bigg] + a^{(1,0)}_{ij} + a^{(1,m)}_{ij} \ . \end{aligned} \tag{44}$$

The factor proportional to the LO coefficients $a^{(0)}_{ij}$ contains usual soft and collinear logarithms. The quantity w denotes the dimensionless value of the soft photon energy cutoff: $E_\gamma < w\sqrt{s}$. It is enough to present four out of the five coefficients because exchanging the positron with the electron momenta leads to the symmetric relationship

$$a_{22}^{(1)} = a_{11}^{(1)}(y_1 \leftrightarrow y_2)\ . \tag{45}$$

The large-angle contributions have been calculated in Ref. [25]. The coefficient proportional to $g^{\mu\nu}$ reads

$$\begin{aligned} a_{00}^{(1,0)} = \frac{1}{y_1\, y_2}\Bigg[&- \frac{q^2(1-q^2)}{2} - y_1 y_2 - \left[q^2 + \frac{2y_1y_2}{1-q^2}\right]\log(q^2) \\ &+ \Bigg\{ \frac{y_1}{2}\left[4 - y_1 - \frac{3(1+q^2)}{1-y_2}\right]\log(\frac{y_1}{q^2}) \\ &- \left[1 + (1-y_2)^2 + \frac{y_1 q^2}{y_2}\right] L(y_1) + (y_1 \leftrightarrow y_2)\Bigg\}\Bigg]\ . \end{aligned} \tag{46}$$

The coefficient in front of the tensor structure $p_1^\mu p_1^\nu$, is given by

$$\begin{aligned} a_{11}^{(1,0)} = \frac{1}{y_1\, y_2}\Bigg[&(1+q^2)^2 \left(\frac{1}{1-y_1} - \frac{1}{1-q^2}\right) - \frac{4(1-y_2)y_1}{1-q^2} \\ &- \frac{2q^2}{1-q^2}\Bigg[(1-y_2)\left(\frac{1}{y_2} + \frac{q^2}{y_1} + \frac{2y_1}{1-q^2}\right) \\ &+ \frac{2q^2}{1-q^2}\Bigg]\log(q^2) - q^2\left[1 + \frac{2}{y_2}\right]\log(\frac{y_1}{q^2}) \\ &- q^2\left[\frac{(2-3y_1)(1-y_2)^2}{y_1(1-y_1)^2}\right]\log(\frac{y_2}{q^2}) \\ &- 2q^2\left[1 + \frac{1}{y_2^2}\right]L(y_1) - 2q^2\left[3 + \frac{2q^2}{y_1} + \frac{q^4}{y_1^2}\right]L(y_2)\Bigg]\ . \end{aligned} \tag{47}$$

For the symmetric tensor structure $(p_1^\mu p_2^\nu + p_2^\mu p_1^\nu)$, one gets

$$\begin{aligned} a_{12}^{(1,0)} = \frac{1}{y_1\, y_2}\Bigg[&- \frac{4q^2 + (y_1-y_2)^2}{1-q^2} \\ &- 2q^2\left[\frac{q^2}{y_1y_2} + \frac{1+q^2-2y_1y_2}{(1-q^2)^2}\right]\log(q^2) + \Bigg\{\frac{q^2}{1-y_1} \\ &- \frac{2q^2}{1-y_2}\left[1 - y_1 + \frac{q^2}{y_2} - \frac{q^2}{2(1-y_2)}\right]\log(\frac{y_1}{q^2}) \\ &- 2q^2\left[1 + \frac{q^2}{y_2} + \frac{q^2}{y_2^2}\right]L(y_1) + (y_1 \leftrightarrow y_2)\Bigg\}\Bigg]\ . \end{aligned} \tag{48}$$

Finally, the antisymmetric coefficient a_{-1}, accompanying $(p_1^\mu p_2^\nu - p_2^\mu p_1^\nu)$, reads

$$\begin{aligned} a_{-1}^{(1,0)} = \frac{q^2}{y_1\, y_2}&\left[\frac{2\log(1-y_1)}{y_1} + \frac{1-q^2}{1-y_1} + \frac{q^2}{(1-y_1)^2}\right] \\ &- (y_1 \leftrightarrow y_2)\ . \end{aligned} \tag{49}$$

The mass-suppressed coefficients $a_{ij}^{(1,m)}$ are given by [26]

$$\begin{aligned} a_{00}^{(1,m)} = \frac{m^2q^2}{y_1^2}&\left[\log(q^2)\log(\frac{y_1^4}{m^4q^2}) + 4\mathrm{Li}_2(1-q^2)\right. \\ &\left. + \mathrm{Li}_2(1-\frac{y_1}{m^2}) - \frac{\pi^2}{6}\right] - \frac{m^2(1-q^2)}{y_1^2}\Bigg[1 - \log(\frac{y_1}{m^2}) \\ &+ \frac{m^2}{y_1}\left(\mathrm{Li}_2(1-\frac{y_1}{m^2}) - \frac{\pi^2}{6}\right)\Bigg] + \frac{q^2}{2}n(y_1, \frac{1-3q^2}{q^2}) \\ &+ (y_1 \leftrightarrow y_2)\ , \end{aligned} \tag{50}$$

and

$$\begin{aligned} a_{11}^{(1,m)} = \frac{q^2}{1-q^2}&\Bigg\{\frac{4m^2}{y_1^2}\Bigg[1 - \log(\frac{y_1}{m^2}) \\ &+ \frac{m^2}{y_1}\left(\mathrm{Li}_2(1-\frac{y_1}{m^2}) - \frac{\pi^2}{6}\right)\Bigg] - n(y_1,1) \\ &+ \frac{2m^2q^2}{y_1(m^2(1-q^2)-y_1)}\Bigg[\frac{1}{q^2}\log(\frac{y_1}{m^2}) + \frac{\log(q^2)}{1-q^2} \\ &+ \left(1 + \frac{m^2}{m^2(1-q^2)-y_1}\right)N(y_1)\Bigg]\Bigg\} + \\ &+ \frac{1}{1-q^2}\Bigg\{\frac{4m^2(1-q^2)}{y_2^2}\Bigg[\log(q^2)\log(\frac{y_2^4}{m^4q^2}) \\ &+ 4\mathrm{Li}_2(1-q^2) + 2\left(\mathrm{Li}_2(1-\frac{y_2}{m^2}) - \frac{\pi^2}{6}\right)\Bigg] \\ &+ \frac{4m^2q^2}{y_2^2}\Bigg[1 - \log(\frac{y_2}{m^2}) + \left(1 + \frac{m^2}{y_2}\right)\Bigg(\mathrm{Li}_2(1-\frac{y_2}{m^2}) \\ &- \frac{\pi^2}{6}\Bigg)\Bigg] - \frac{1-2q^4}{q^2}n(y_2, \frac{3-8q^2+6q^4}{1-2q^4}) \\ &+ \frac{2m^2}{y_2(m^2(1-q^2)-y_2)}\Bigg[\frac{1}{q^2}\log(\frac{y_2}{m^2}) + \frac{\log(q^2)}{1-q^2} \\ &+ \left(3 + \frac{m^2}{m^2(1-q^2)-y_2}\right)N(y_2)\Bigg]\Bigg\}\ , \end{aligned} \tag{51}$$

and

$$\begin{aligned} a_{12}^{(1,m)} = \frac{q^2}{1-q^2}&\Bigg\{\frac{4m^2}{y_1^2}\Bigg[1 - \log(\frac{y_1}{m^2}) \\ &+ \left(\frac{1}{2} + \frac{m^2}{y_1}\right)\left(\mathrm{Li}_2(1-\frac{y_1}{m^2}) - \frac{\pi^2}{6}\right)\Bigg] \\ &- \frac{1-q^2}{q^2}n(y_1, \frac{1}{1-q^2}) + \frac{2m^2}{y_1(m^2(1-q^2)-y_1)} \\ &\times\Bigg[\frac{1}{q^2}\log(\frac{y_1}{m^2}) + \frac{\log(q^2)}{1-q^2} \\ &+ \left(2 + \frac{m^2}{m^2(1-q^2)-y_1}\right)N(y_1)\Bigg]\Bigg\} + (y_1 \leftrightarrow y_2)\ . \end{aligned} \tag{52}$$

The asymmetric coefficient does not get mass corrections:

$$a_{-1}^{(1,m)} = 0\ . \tag{53}$$

These results are written in terms of the function

$$L(y_i) = \mathrm{Li}_2(-\frac{y_i}{q^2}) - \mathrm{Li}_2(1-\frac{1}{q^2}) + \log(q^2+y_i)\log(\frac{y_i}{q^2}) \ , \quad (54)$$

where Li_2 is the Spence or dilogarithm function, and the functions $n(y_i,z)$ and $N(y_i)$, which are defined through

$$n(y_i,z) = \frac{m^2}{y_i(m^2-y_i)}\left[1+z\ \log(\frac{y_i}{m^2})\right] + \frac{m^2}{(m^2-y_i)^2}\log(\frac{y_i}{m^2}) \ , \quad (55)$$

and

$$N(y_i) = \log(q^2)\log(\frac{y_i}{m^2}) + \mathrm{Li}_2(1-q^2) + \mathrm{Li}_2(1-\frac{y_i}{m^2}) - \frac{\pi^2}{6} \ . \quad (56)$$

The apparent singularity of the function $n(y_i,z)$ inside the limits of phase space is compensated by the zero in the numerator. In the region y_i close to m^2 it behaves as

$$n(y_i,z)\big|_{y_i\to m^2} = \frac{1}{y_i}\left[1+z\ \log(\frac{y_i}{m^2})\right] - \frac{1}{m^2}\sum_{n=0}\left(\frac{1}{n+2}+\frac{z}{n+1}\right)\left(1-\frac{y_i}{m^2}\right)^n \ . \quad (57)$$

Similarly, the function $N(y_i)$ guarantees that the coefficients $a_{ij}^{(1)}$ are finite in the limit $y_i \to m^2(1-q^2)$:

$$\frac{m^2 N(y_i)}{m^2(1-q^2)-y_i}\Bigg|_{y_i\to m^2(1-q^2)} = -\frac{\log(1-q^2)}{q^2} - \frac{\log(q^2)}{1-q^2} \ . \quad (58)$$

Virtual and soft corrections to IFS

The virtual plus soft photon corrections of the initial-state and final-state vertex (see Eq.(37)) to FSR and ISR, respectively, can be written as [137,138]

$$d\sigma_{\mathrm{IFS}}^{\mathrm{V+S}} = \frac{\alpha}{\pi}\left[\delta^{\mathrm{V+S}}(w)\, d\sigma_{\mathrm{FSR}}^{(0)}(s) + \eta^{\mathrm{V+S}}(s',w)\, d\sigma_{\mathrm{ISR}}^{(0)}(s')\right] \ , \quad (59)$$

where $d\sigma_{\mathrm{FSR}}^{(0)}$ and $d\sigma_{\mathrm{ISR}}^{(0)}$ are the leading order FSR and ISR differential cross sections, respectively, $w = E_\gamma^{\mathrm{cut}}/\sqrt{s}$, with E_γ^{cut} the maximal energy of the soft photon in the e^+e^- c.m. rest frame, and s' corresponds to the squared mass of the $h\bar{h}\gamma$ system. The function $\delta^{\mathrm{V+S}}(w)$ is independent of the final state. In the limit $m_e^2 \ll s$:

$$\delta^{\mathrm{V+S}}(w) = 2\left[(L-1)\log(2w) + \frac{3}{4}L - 1 + \frac{\pi^2}{6}\right] \ , \quad (60)$$

where $L = \log(s/m_e^2)$. For two pions in the final state, the function $\eta^{\mathrm{V+S}}(s',w)$ is given by

$$\begin{aligned}\eta^{\mathrm{V+S}}(s',w) &= -2\left[\frac{1+\beta_\pi^2}{2\beta_\pi}\log(t_\pi)+1\right] \\ &\times \left[\log(2w)+1+\frac{s'}{s'-s}\log\left(\frac{s}{s'}\right)\right] + \log\left(\frac{m_\pi^2}{s'}\right) \\ &- \frac{1+\beta_\pi^2}{\beta_\pi}\left[2\mathrm{Li}_2(1-t_\pi)+\log(t_\pi)\log(1+t_\pi)-\frac{\pi^2}{2}\right] \\ &- \frac{2+\beta_\pi^2}{\beta_\pi}\log(t_\pi) - 2 \ , \end{aligned} \quad (61)$$

where

$$\beta_\pi = \sqrt{1-\frac{4m_\pi^2}{s'}} \ , \qquad t_\pi = \frac{1-\beta_\pi}{1+\beta_\pi} \ . \quad (62)$$

The function $\eta^{\mathrm{V+S}}(s',w)$ is equivalent to the familiar correction factor derived in [139] for the reaction $e^+e^- \to \pi^+\pi^-\gamma$ in the framework of sQED (see also [140]) in the limit $s \to s'$:

$$\log(2w)+1+\frac{s'}{s'-s}\log\left(\frac{s}{s'}\right)\Bigg|_{s\to s'} = \log(2w') \quad (63)$$

with $w' = E_\gamma^{\mathrm{cut}}/\sqrt{s'}$. The factor in the right hand side of Eq.(63) for $s \neq s'$ arises from defining the soft photon cutoff in the e^+e^- laboratory frame.

Correspondingly, the function $\eta^{\mathrm{V+S}}(s',w)$ for two muons in the final state reads

$$\begin{aligned}\eta^{\mathrm{V+S}}(s',w) &= -2\left[\frac{1+\beta_\mu^2}{2\beta_\mu}\log(t_\mu)+1\right] \\ &\times \left[\log(2w)+1+\frac{s'}{s'-s}\log\left(\frac{s}{s'}\right)\right] + \log\left(\frac{m_\mu^2}{s'}\right) \\ &- \frac{1+\beta_\mu^2}{2\beta_\mu}\left[4\mathrm{Li}_2(1-t_\mu)-2\log(t_\mu)\log\left(\frac{1+\beta_\mu}{2}\right)-\pi^2\right] \\ &- \frac{1}{\beta_\mu}\left[\frac{3}{3-\beta_\mu^2}+\beta_\mu^2\right]\log(t_\mu) - 2 \ , \end{aligned} \quad (64)$$

where

$$\beta_\mu = \sqrt{1-\frac{4m_\mu^2}{s'}} \ , \qquad t_\mu = \frac{1-\beta_\mu}{1+\beta_\mu} \ . \quad (65)$$

Real corrections

Matrix elements for the emission of two real photons

$$e^+(p_1) + e^-(p_2) \to \mathrm{hadrons}\,(Q) + \gamma(k_1) + \gamma(k_2) \ , \quad (66)$$

are calculated in PHOKHARA following the helicity amplitude method with the conventions introduced in [141, 142]. The Weyl representation for fermions is used where the Dirac matrices

$$\gamma^\mu = \begin{pmatrix} 0 & \sigma_+^\mu \\ \sigma_-^\mu & 0 \end{pmatrix} \ , \qquad \mu = 0,1,2,3 \ , \quad (67)$$

are given in terms of the unit 2×2 matrix I and the Pauli matrices $\sigma_i, i = 1, 2, 3$, with $\sigma^\mu_\pm = (I, \pm\sigma_i)$. The contraction of any four-vector a^μ with the γ^μ matrices has the form

$$\not{a} = a_\mu \gamma^\mu = \begin{pmatrix} 0 & a^+ \\ a^- & 0 \end{pmatrix} , \tag{68}$$

where the 2×2 matrices $a^\pm$ are given by

$$a^\pm = a^\mu \sigma^\pm_\mu = \begin{pmatrix} a^0 \mp a^3 & \mp(a^1 - ia^2) \\ \mp(a^1 + ia^2) & a^0 \pm a^3 \end{pmatrix} . \tag{69}$$

The helicity spinors u and v for a particle and an antiparticle of four-momentum $p = (E, \mathbf{p})$ and helicity $\lambda = \pm 1/2$ are given by

$$\begin{aligned} u(p, \lambda = \pm 1/2) &= \begin{pmatrix} \sqrt{E \mp |\mathbf{p}|}\, \chi(\mathbf{p}, \pm) \\ \sqrt{E \pm |\mathbf{p}|}\, \chi(\mathbf{p}, \pm) \end{pmatrix} \equiv \begin{pmatrix} u_I \\ u_{II} \end{pmatrix} , \\ v(p, \lambda = \pm 1/2) &= \begin{pmatrix} \mp\sqrt{E \pm |\mathbf{p}|}\, \chi(\mathbf{p}, \mp) \\ \pm\sqrt{E \mp |\mathbf{p}|}\, \chi(\mathbf{p}, \mp) \end{pmatrix} \equiv \begin{pmatrix} v_I \\ v_{II} \end{pmatrix} . \end{aligned} \tag{70}$$

The helicity eigenstates $\chi(\mathbf{p}, \lambda)$ can be expressed in terms of the polar and azimuthal angles of the momentum vector $\mathbf{p}$ as

$$\begin{aligned} \chi(\mathbf{p}, +) &= \begin{pmatrix} \cos(\theta/2) \\ e^{i\phi} \sin(\theta/2) \end{pmatrix} , \\ \chi(\mathbf{p}, -) &= \begin{pmatrix} -e^{-i\phi} \sin(\theta/2) \\ \cos(\theta/2) \end{pmatrix} . \end{aligned} \tag{71}$$

Finally, complex polarization vectors in the helicity basis are defined for the real photons:

$$\begin{aligned} \varepsilon^\mu(k_i, \lambda_i = \pm) = \frac{1}{\sqrt{2}} \big(0, &\mp \cos\theta_i \cos\phi_i + i \sin\phi_i, \\ &\mp \cos\theta_i \sin\phi_i - i \cos\phi_i, \pm \sin\theta_i\big) , \end{aligned} \tag{72}$$

with $i = 1, 2$.

Phase space

One of the key ingredients of any Monte Carlo simulation is an efficient generation of the phase space. The generation of the multiparticle phase space in PHOKHARA is based on the following Lorentz-invariant representation:

$$\begin{aligned} d\Phi_{m+n}(p_1, p_2; k_1, \cdot, k_m, q_1, \cdot, q_n) = \\ d\Phi_m(p_1, p_2; Q, k_1, \cdot, k_m) d\Phi_n(Q; q_1, \cdot, q_n) \frac{dQ^2}{2\pi} , \end{aligned} \tag{73}$$

where p_1 and p_2 are the four-momenta of the initial particles, $k_1 \dots k_m$ are the four momenta of the emitted photons and $q_1 \dots q_n$, with $Q = \sum q_i$, label the four-momenta of the final state hadrons.

When two particles of the same mass are produced in the final state, $q_i^2 = M^2$, their phase space is given by

$$d\Phi_2(Q; q_1, q_2) = \frac{\sqrt{1 - \frac{4M^2}{Q^2}}}{32\pi^2} d\Omega , \tag{74}$$

where $d\Omega$ is the solid angle of one of the final state particles at, for instance, the Q^2 rest frame.

Single photon emission is described by the corresponding leptonic part of phase space

$$d\Phi_2(p_1, p_2; Q, k_1) = \frac{1 - q^2}{32\pi^2} d\Omega_1 , \tag{75}$$

with $q^2 = Q^2/s$ and $d\Omega_1$ the solid angle of the emitted photon at the e^+e^- rest frame. The polar angle θ_1 is defined with respect to the positron momentum p_1. In order to make the Monte Carlo generation more efficient, the following substitution is performed:

$$\cos\theta_1 = \frac{1}{\beta} \tanh(\beta\, t_1) , \quad t_1 = \frac{1}{2\beta} \log \frac{1 + \beta\cos\theta_1}{1 - \beta\cos\theta_1} , \tag{76}$$

with $\beta = \sqrt{1 - 4m_e^2/s}$, which accounts for the collinear emission peaks

$$\frac{d\cos\theta_1}{1 - \beta^2 \cos^2\theta_1} = dt_1 . \tag{77}$$

Then, the azimuthal angle and the new variable t_1 are generated flat.

Considering the emission of two real photons in the c.m. of the initial particles, the four-momenta of the positron, the electron and the two emitted photons are given by

$$\begin{aligned} &p_1 = \frac{\sqrt{s}}{2}(1, 0, 0, \beta) , \qquad p_2 = \frac{\sqrt{s}}{2}(1, 0, 0, -\beta) , \\ &k_1 = w_1 \sqrt{s}(1, \sin\theta_1 \cos\phi_1, \sin\theta_1 \sin\phi_1, \cos\theta_1) , \\ &k_2 = w_2 \sqrt{s}(1, \sin\theta_2 \cos\phi_2, \sin\theta_2 \sin\phi_2, \cos\theta_2) , \end{aligned} \tag{78}$$

respectively. The polar angles θ_1 and θ_2 are again defined with respect to the positron momentum p_1. Both photons are generated with energies larger than the soft photon cutoff: $w_i > w$ with $i = 1, 2$. At least one of these exceeds the minimal detection energy: $w_1 > E_\gamma^{\min}/\sqrt{s}$ or $w_2 > E_\gamma^{\min}/\sqrt{s}$. In terms of the solid angles $d\Omega_1$ and $d\Omega_2$ of the two photons and the normalized energy of one of them, e.g. w_1, the leptonic part of phase space reads

$$\begin{aligned} d\Phi_3(p_1, p_2; Q, k_1, k_2) = \frac{1}{2!} \frac{s}{4(2\pi)^5} \\ \times \frac{w_1 w_2^2}{1 - q^2 - 2w_1} dw_1\, d\Omega_1\, d\Omega_2 , \end{aligned} \tag{79}$$

where the limits of the phase space are determined from the constraint

$$q^2 = 1 - 2(w_1 + w_2) + 2w_1 w_2 (1 - \cos\chi_{12}) , \tag{80}$$

with χ_{12} being the angle between the two photons

$$\cos\chi_{12} = \sin\theta_1 \sin\theta_2 \cos(\phi_1 - \phi_2) + \cos\theta_1 \cos\theta_2 . \tag{81}$$

Again, the matrix element squared contains several peaks, soft and collinear, which should be softened by choosing suitable substitutions in order to achieve an efficient Monte Carlo generator. The leading behaviour of the matrix element squared is given by $1/(y_{11}\, y_{12}\, y_{21}\, y_{22})$, where

$$y_{ij} = \frac{2k_i \cdot p_j}{s} = w_i(1 \mp \beta \cos\theta_i) \ . \tag{82}$$

In combination with the leptonic part of phase space, we have

$$\frac{d\Phi_3(p_1, p_2; Q, k_1, k_2)}{y_{11}\, y_{12}\, y_{21}\, y_{22}} \sim \frac{dw_1}{w_1(1 - q^2 - 2w_1)} \times \frac{d\Omega_1}{1 - \beta^2 \cos^2\theta_1} \frac{d\Omega_2}{1 - \beta^2 \cos^2\theta_2} \ . \tag{83}$$

The collinear peaks are then flattened with the help of Eq.(76), with one change of variables for each photon polar angle. The remaining soft peak, $w_1 \to w$, is reabsorbed with the following substitution

$$w_1 = \frac{1 - q^2}{2 + e^{-u_1}} \ , \quad u_1 = \log \frac{w_1}{1 - q^2 - 2w_1} \ , \tag{84}$$

or

$$\frac{dw_1}{w_1(1 - q^2 - 2w_1)} = \frac{du_1}{1 - q^2} \ , \tag{85}$$

where the new variable u_1 is generated flat. Multi-channeling is used to absorb simultaneously the soft and collinear peaks, and the peaks of the form factors.

NLO cross section and theoretical uncertainty

The LO and NLO predictions for the differential cross section of the process $e^+e^- \to \pi^+\pi^-\gamma(\gamma)$ at DAΦNE energies, $\sqrt{s} = 1.02$ GeV, are presented in Figure 8 as a function of the invariant mass of the hadronic system $M_{\pi\pi}$. We choose the same kinematical cuts as in the small angle analysis of KLOE [68]; pions are restricted to be in the central region, $50^o < \theta_\pi < 130^o$, with $|p_T| > 160$ MeV or $|p_z| > 90$ MeV, the hard photon is not tagged and the sum of the momenta of the two pions, which flows in the opposite direction to the photon's momenta, is close to the beam ($\theta_{\pi\pi} < 15^o$ or $\theta_{\pi\pi} > 165^o$). The track mass, which is calculated from the equation

$$\left(\sqrt{s} - \sqrt{|\boldsymbol{p}_{\pi^+}|^2 + M_{\rm trk}^2} - \sqrt{|\boldsymbol{p}_{\pi^-}|^2 + M_{\rm trk}^2}\right)^2 - (\boldsymbol{p}_{\pi^+} + \boldsymbol{p}_{\pi^-})^2 = 0 \ , \tag{86}$$

lies within the limits 130 MeV$< M_{\rm trk} < 220$ MeV and $M_{\rm trk} < (250 - 105\sqrt{1 - (M_{\pi\pi}^2/0.85)^2})$ MeV, with $M_{\pi\pi}$ in GeV, in order to reject $\mu^+\mu^-$ and $\pi^+\pi^-\pi^0$ events. The cut on the track mass, however, does not have any effect for single photon emission, as obviously $M_{\rm trk} = m_\pi$ for such events.

The lower plot in Figure 8 shows the relative size, with respect to the LO prediction, of FSR at LO, ISR corrections at NLO, and IFS contributions. The NLO ISR radiative corrections are almost flat and of the order of -8%, FSR is clearly below 1%, while IFS corrections are also small although they become of the order of a few per cent at high values of $M_{\pi\pi}$.

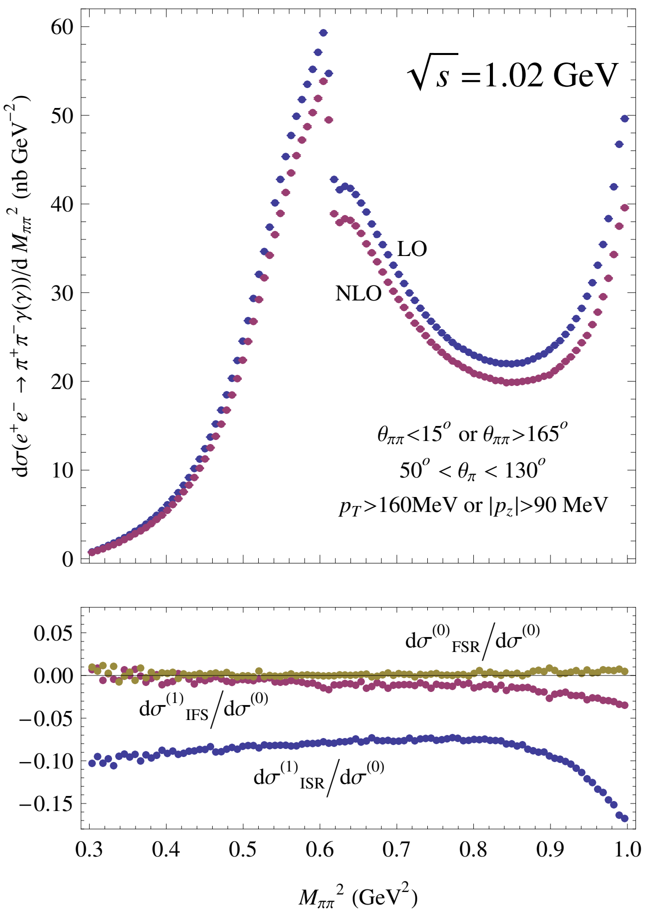

Fig. 8. Differential cross section for the process $e^+e^- \to \pi^+\pi^-\gamma$ at LO and NLO for $\sqrt{s} = 1.02$ GeV. The cuts are the same as in the small angle analysis of KLOE, including the cut on the track mass. The lower plot shows the relative size of FSR at LO, ISR at NLO and IFS contributions with respect to the full LO prediction.

To estimate the systematic uncertainty of the NLO prediction, we observe that leading logarithmic two-loop $\mathcal{O}(\alpha^2)$ corrections and the associate real emission are not included. For samples with untagged photons the process $e^+e^- \to e^+e^-\pi^+\pi^-$ might also become a sizable background. This process, however, can be simulated with the Monte Carlo event generator EKHARA [143,144]. Its contribution depends on the pion pair invariant mass, ranges from $0.1 - 0.8\%$ for the KLOE event selection, and has been taken into account in the KLOE analysis [68].

From naïve exponentiation one expects that LL corrections at next-to-next-to-leading order (NNLO) are of the order of $\frac{1}{2}(\frac{3}{2}(\alpha/\pi)\log(s/m_e^2))^2 \approx 0.1$–$0.2\%$ for inclusive observables. For less inclusive distributions, a larger error is expected. The conservative estimate of the accuracy of PHOKHARA from ISR is 0.5%. This has been confirmed by comparisons with KKMC [145,146], where the biggest observed difference is about 0.3% in the invariant mass regions, which are not close to the nominal energies of the experiments. Improving the accuracy of PHOKHARA below 0.5%, however, will be required to meet the growing experimental requirements in the near future.

4.2.4 FSR beyond sQED∗VMD model

The model of the FSR emission from pions described in details in Sections 4.2.1 and 4.2.3 will be called for short the sQED∗VMD model. A question arises how well it can reflect the data. As it is shown in [10], the first two terms in the expansion of the FSR amplitude as a function of $k^0/\sqrt{Q^2}$ (i.e. the divergence and the constant) are fully given by the pion form factor. Thus only for a hard photon emission one could expect that going beyond this approximation is necessary. Moreover, the pion form factor is extremely big in the ρ resonance region and thus the validity of this approximation is further extended. In the kinematical regions, where there are resonance contributions not contained in the pion form factor and also near the $\pi^+\pi^-$ threshold, where the emitted photon is hard and the pion form factor is relatively small, going beyond the sQED∗VMD model is necessary and one needs a more general description of the amplitude $M(\gamma^*(Q) \to \gamma(k) + \pi^+(q_1) + \pi^-(q_2))$.

In the general case the amplitude of the reaction $\gamma^*(Q) \to \gamma(k) + \pi^+(q_1) + \pi^-(q_2)$ depends on three 4-momenta, which can be chosen as Q, k, and $l \equiv q_1 - q_2$. The second-rank Lorentz tensor $M^{\mu\nu}(Q,k,l)$, that describes the FSR amplitude, can be decomposed through ten independent tensors [147,148]. Taking into account the charge conjugation symmetry of the S-matrix element $(\langle\gamma(k),\pi^+(q_1)\pi^-(q_2)|S|\gamma^*(Q)\rangle = \langle\gamma(k),\pi^-(q_1)\pi^+(q_2)|S|\gamma^*(Q)\rangle)$, the photon crossing symmetry ($Q \leftrightarrow -k$ and $\mu \leftrightarrow \nu$) and the gauge invariance conditions $Q_\mu M^{\mu\nu}(Q,k,l) = 0$ and $M_F^{\mu\nu}(Q,k,l)k_\nu = 0$, the number of the independent tensors decreases to five. For a final real photon, i.e. $k^2 = 0$ and $k^\nu\epsilon_\nu = 0$ (ϵ_ν is the polarization vector of the final photon) and the initial virtual photon produced in e^+e^- annihilation ($Q^2 \geq 4m_\pi^2$), the FSR tensor can be rewritten in the terms of three gauge invariant tensors[147,148]

$$M^{\mu\nu}(Q,k,l) = \tau_1^{\mu\nu} f_1 + \tau_2^{\mu\nu} f_2 + \tau_3^{\mu\nu} f_3, \tag{87}$$

where the gauge invariant tensors $\tau_i^{\mu\nu}$ read

$$\begin{aligned}
\tau_1^{\mu\nu} &= k^\mu Q^\nu - g^{\mu\nu} k\cdot Q, \\
\tau_2^{\mu\nu} &= k\cdot l(l^\mu Q^\nu - g^{\mu\nu} k\cdot l) + l^\nu(k^\mu k\cdot l - l^\mu k\cdot Q), \\
\tau_3^{\mu\nu} &= Q^2(g^{\mu\nu} k\cdot l - k^\mu l^\nu) + Q^\mu(l^\nu k\cdot Q - Q^\nu k\cdot l).
\end{aligned} \tag{88}$$

It thus follows that the evaluation of the FSR tensor amounts to the calculation of the scalar functions $f_i(Q^2, Q\cdot k, k\cdot l) \quad (i = 1,2,3)$.

As it is clear from the above discussion, the extraction of the pion form factor from radiative return experiments is a demanding task. The main problem is that in the same experiments one has to test the models describing the pion-photon interactions (see Section 4.3) and to extract the pion form factor needed for the evaluation of the muon anomalous magnetic moment. Fortunately, there are event selections, which naturally suppress the FSR contributions, independently of their nature. These were already discussed in Section 4.2.1 in the context of the sQED∗VMD model.

Extensive theoretical studies of the role of the FSR emission beyond the sQED∗VMD model were performed [31,41,43,45,44]. They are important mainly for the KLOE measurements at DAPHNE as at B- meson factories the FSR is naturally suppressed and the accuracy needed in its modeling is by far less demanding than for the KLOE purposes.

For DAPHNE, running on or near the ϕ resonance, the following mechanisms of the $\pi^+\pi^-$ final state photon emission have to be considered:

bremsstrahlung process

$$e^+ + e^- \to \pi^+ + \pi^- + \gamma\ , \tag{89}$$

which is modelled by sQED∗VMD;

ϕ direct decay

$$e^+ + e^- \to \phi \to (f_0; f_0 + \sigma)\gamma \to \pi^+ + \pi^- + \gamma\ , \tag{90}$$

and double resonance process

$$e^+ + e^- \to (\phi; \omega') \to \rho\pi \to \pi^+ + \pi^- + \gamma\ . \tag{91}$$

The resonance chiral theory (RχT) [149,150] was used in [43,44] to estimate the contributions beyond sQED∗VMD. They were implemented at the leading order into an event generator FASTERD [45]. Having in mind that at present the models still await accurate experimental tests, in the event generator FASTERD other models [151,152] were also implemented. To include both next-to-leading-order radiative corrections and the discussed mechanisms of the FSR production, a part of the FASTERD code, based on models [151,152], was implemented by O. Shekhovtsova in PHOKHARA6.0 (PHOKHARA6.1 [153]) and the studies presented below are based on this code. The model used there, even if far from an ideal, is the best tested model available in literature.

We shortly describe main features of the models used to describe processes contributing to FSR photon emission listed above. For more detailed description and the calculation of the function f_i we refer the reader to [31, 41,45] (see also references therein).

The sQED∗VMD part gives contributions to f_1 and f_2.

The ϕ direct decay is assumed to proceed through the intermediate scalar meson state: $\phi \to (f_0 + \sigma)\gamma \to \pi\pi\gamma$. Various models are proposed to describe the ϕ-scalar-γ vertex: either it is the direct decay $\phi \to (scalar)\gamma$ or the vertex is generated dynamically through the loop of the charged kaons. As shown in [41], in the framework of any model the ϕ direct decay affects only the form factor f_1 of Eq. (87).

The double resonance contribution consists of the off-shell ϕ meson decay into ($\rho^\pm\pi^\mp$) and subsequent decay $\rho \to \pi\gamma$. In the energy region around 1 GeV the tail of the excited ω meson can also play a role and $\gamma^* \to \omega' \to \rho\pi$

has to be considered. The double resonance mechanism affects all three form factors f_i of Eq. (87).

Assuming isospin symmetry, this part can be deduced from the measurement of the neutral pion pair production. Various models [151,152] were confronted with data by KLOE [154] for the neutral mode. The model, which was reproducing the data in the best way was adopted to be used for the charged pion pair production relying on the isospin symmetry [153].

In [31] it was shown that an important tool for testing of the various models of the FSR emission is the charge asymmetry. At the leading order it originates from the fact that the pion pair couples to even (odd) number of photons if the final state photon is emitted from the final (initial) state. The interference diagrams do not give contribution to the integrated cross section for C–even event selections but produce asymmetry in the angular distribution. The definitions and experimental studies based on the charge asymmetry are presented in Section 4.3.2

Few strategies can be adopted how to profit in the best way from the KLOE data taken on and off peak. The 'easiest' part is to look for the event selections, where the FSR contributions are negligible. This was performed by KLOE [68] (see Section 4.4.1), giving important information on the pion form factor relevant for the prediction of the hadronic contributions to the muon anomalous magnetic moment a_μ. Typical contributions of the FSR (1%-4%) to the differential cross section (Fig. 8 and 9) allow for excellent control on the accuracy of these corrections. One disadvantage of using this event selection is that it does not allow to perform measurements near the pion production threshold.

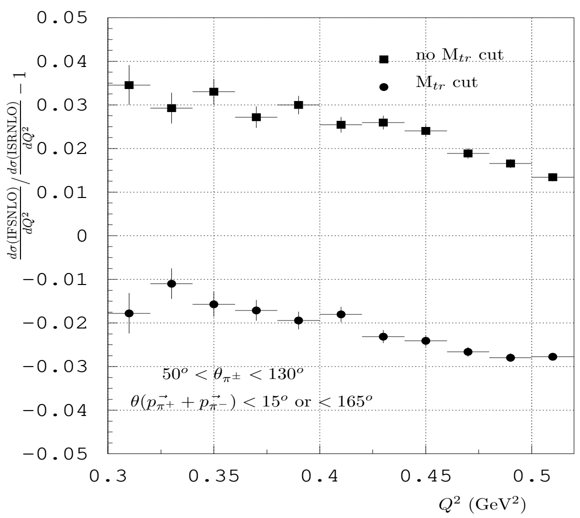

Fig. 9. Relative contribution of the FSR to the differential cross section of the reaction $e^+e^- \to \pi^+\pi^-\gamma(\gamma)$ for $\sqrt{s} = m_\phi$ and low invariant masses of pion pairs. KLOE small angle event selection [68] was used and for this event selection the relative contribution of the FSR is almost identical also for off peak cross section. The effect of mass track cut (see Section 4.4.1) is shown. ISRNLO refers to initial state correction at next to leading order (NLO). IFSNLO cross section contains the final states emission at NLO.

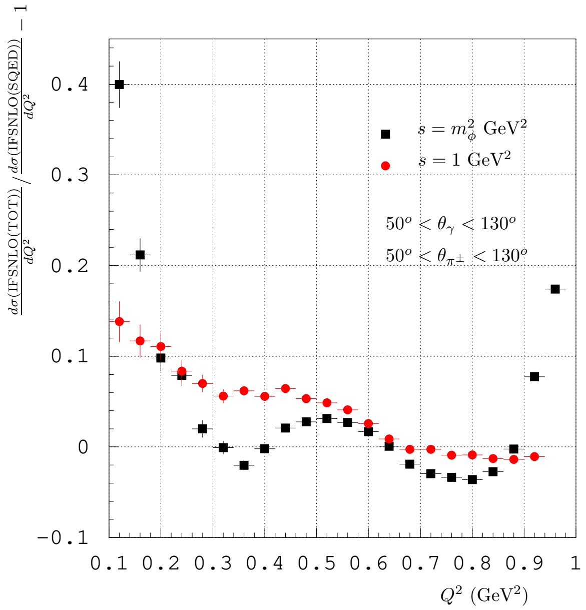

Fig. 10. The contributions of FSR beyond sQED$*$VMD approximation (see eq. 90 and 91) for large angle KLOE event selection [155,156] for $\sqrt{s} = m_\phi$ and for $\sqrt{s} = 1$GeV.

The next step, partly discussed in Section 4.3.2, is to confront the models based on the isospin symmetry and the neutral channel data with charged pion data taken off-peak, where the contributions from models beyond the sQED$*$VMD approximation are relatively small (Fig. 10). For the off-peak data [155] the region below $Q^2 = 0.3$GeV^2 can be covered experimentally, however, the small statistics in this region makes it difficult to perform high-precision tests of the models. For this analysis an accurate knowledge of the pion form factor at the nominal energy of the experiment is important as it defines the sQED$*$VMD predictions and the FSR corrections (Fig. 11) are sizable.

The last step, which allows for the most accurate FSR model testing and profits from the knowledge of the pion form factor from previous analysis, is the on-peak large angle measurement. The large FSR corrections coming from sources beyond the sQED$*$VMD approximation (Fig. 10 and 11) make these data [156] the most valuable source of information on these models. In this case the accumulated data set is much larger than the off-peak data and one is able to cover also the region below $Q^2 = 0.3$GeV^2.

4.3 Experiment confronting theory

4.3.1 Study of the process $e^+e^- \to \pi^+\pi^-\gamma$ with FSR with CMD-2 detector at VEPP-2M

A study of the process $e^+e^- \to \pi^+\pi^-\gamma$ with photon radiation from the final state pions can be used to answer the question whether one can treat pions as point-like particles and apply scalar QED in the calculation of the radiative corrections to the cross section. In particular, one can compare the photon spectra obtained using scalar QED with the ones found in data.

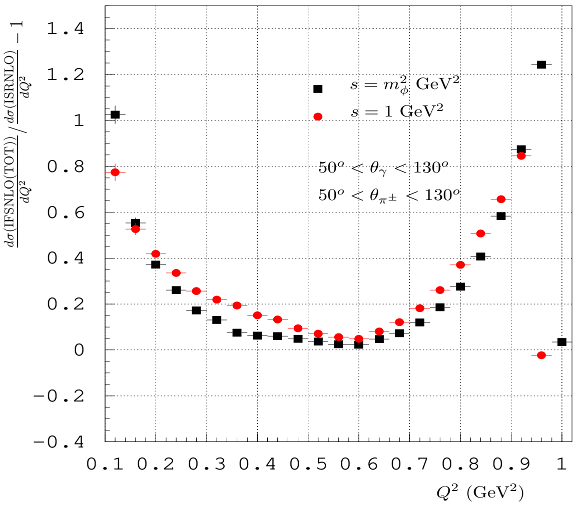

Fig. 11. Relative contribution of FSR to the differential cross section of the reaction $e^+e^- \to \pi^+\pi^-\gamma(\gamma)$ for $\sqrt{s} = m_\phi$ and for $\sqrt{s} = 1$GeV. KLOE large angle event selection [155,156] was used.

The radiative corrections due to photon emission in the final state contribute about 1% to the cross section. The hadronic contribution to (g-2)/2 of the muon from the process $e^+e^- \to \pi^+\pi^-$ amounts to 50 ppm, while the anomalous magnetic moment of the muon was measured in the E821 experiment at BNL with an accuracy of 0.5 ppm [73]. Therefore the theoretical uncertainty on the cross section calculation of the of the process $e^+e^- \to \pi^+\pi^-\gamma$ should be better than 1% to be able to neglect the error of this contribution with respect to the 0.5 ppm. These facts are the main motivation to study this process.

In the following, the preliminary results of the analysis of the process $e^+e^- \to \pi^+\pi^-\gamma$ with final state radiation are presented. The analysis is based on an integrated luminosity of about 1.2 pb^{-1}. The data were collected in the c.m. energy range from 720 MeV to 780 MeV by the CMD-2 detector. Pions were considered as point-like objects and scalar QED was applied to describe the photon radiation in the final state.

Event selection

For the analysis, the data were taken in a c.m. energy range from 720 MeV to 780 MeV, with the photon detected in the CsI calorimeter of the CMD-2 experiment. Events from the processes $e^+e^- \to e^+e^-\gamma$, $e^+e^- \to \mu^+\mu^-\gamma$ have a very similar signature in the detector compared to $e^+e^- \to \pi^+\pi^-\gamma$ events. In addition, the cross section of the process $e^+e^- \to \pi^+\pi^-\gamma$ with a final state photon is more than ten times smaller than the one for the similar process with a photon radiated in the initial state. On the other hand, the cross section of the process $e^+e^- \to \pi^+\pi^-\gamma$ has a resonant shape in the studied energy region due to the presence of the ρ-meson. This allows to enhance significantly the fraction of events $e^+e^- \to \pi^+\pi^-\gamma$ with final state photons. Selecting events below the ρ-resonance, the photon radiation from the initial state will decrease the cross section, whereas the process with a final state photon has practically no energy dependence.

Several curves describing the ratio $\sigma^{FSR+ISR}_{\pi^+\pi^-\gamma}/\sigma^{ISR}_{\pi^+\pi^-\gamma}$ plotted against the c.m.energy are presented in Fig. 12 for different energy thresholds of photon detection in the calorimeter. It is clearly visible that the optimal energy range to be used in this study goes from 720 MeV up to 780 MeV.

It can also be seen that the cross section ratio increases with the energy threshold for photons. The fraction of $\pi^+\pi^-\gamma$ events with a final state radiation photon increases with photon energy. This allows to enrich the spectrum of $\pi^+\pi^-\gamma$ events with FSR. Of special interest is the part of the photon spectra in which the photon energy is of the same order as the pion mass or larger.

A typical $\pi^+\pi^-\gamma$ event in the CMD-2 detector has two tracks in the drift chamber with two associated clusters in the CsI calorimeter and a third cluster representing the radiated photon. To suppress multiphoton events and significantly cut off the collinear $\pi^+\pi^-$ events the following requirements were applied: The angle between the photon direction and the missing momentum must be larger than 1 rad and the angle between anyof the tracks and the photon direction must be larger than 0.2 rad.

To suppress $e^+e^-\gamma$ events, a parameter $W = p/E$ was used, in which the particle momentum p (measured in the drift chamber) is divided by the energy E (measured in the CsI calorimeter). Simulation results are presented in Fig. 13. The condition $W < 0.4$ reduces the electron contribution to the level of $\sim 1\%$. The squared invariant mass for electrons, muons and pions is plotted in Fig. 14. The condition $M^2 > 10000$ MeV^2 rejects additional electrons and muons by a factor of 1.5. About 1% of pion events are lost.

Preliminary results of the analysis

The histogram of the photon spectrum from the CMD-2 experimental data is presented in Fig. 15. The histogram represents the simulation, while the points with error bars represent the experimental result. Vertical dotted lines divide the plot area into three zones. The inscription inside each zone indicates the fraction of $\pi^+\pi^-\gamma$ events with final state radiation with respect to the total number of events. The number of the simulated events was normalized to the experimental one. The average deviation between the two distributions was found to be $(-2.1 \pm 2.3)\%$. As a result, one can conclude that there are no indications that photon radiation by pions needs to be described beyond the scalar QED framework. Pions can be treated as point-like objects and the application of the scalar QED is found to be valid within the stated accuracy. Unfortunately, lack of statistics in the energy range under study does not allow to check this assumption with better accuracy. Forthcoming results from VEPP-2000 will significantly improve the statistical error.

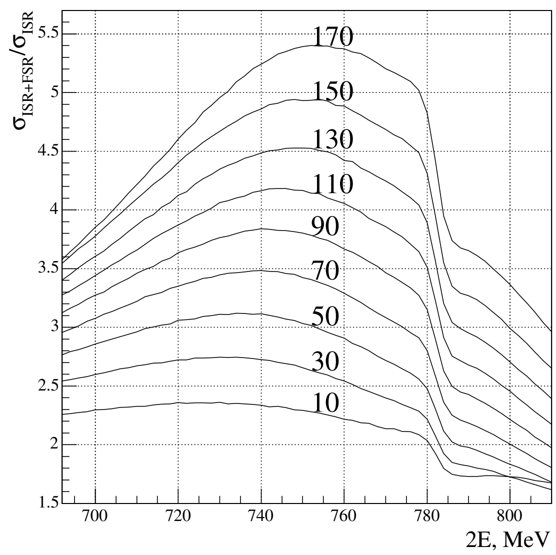

(a)

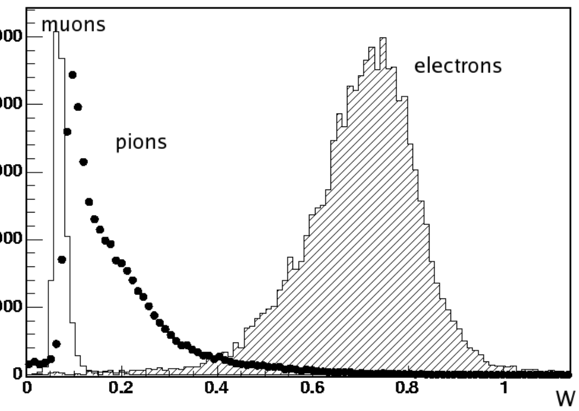

(b)

Fig. 12. (a) Ratio $\sigma_{ISR+FSR}/\sigma_{ISR}$ vs c.m.energy. The set of curves indicates how this ratio depends on the detection threshold energy for photons. The threshold energy in MeV is stated over the curves.

Fig. 13. (b) Distributions of the parameter W for events of the processes $e^+e^- \to \pi^+\pi^-\gamma$, $e^+e^- \to \mu^+\mu^-\gamma$ and $e^+e^- \to e^+e^-\gamma$, for a c.m.-energy of 780 MeV.

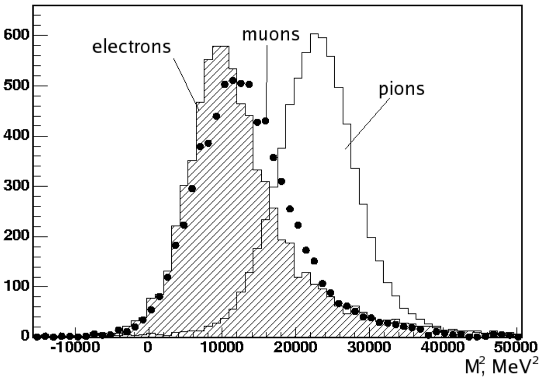

(a)

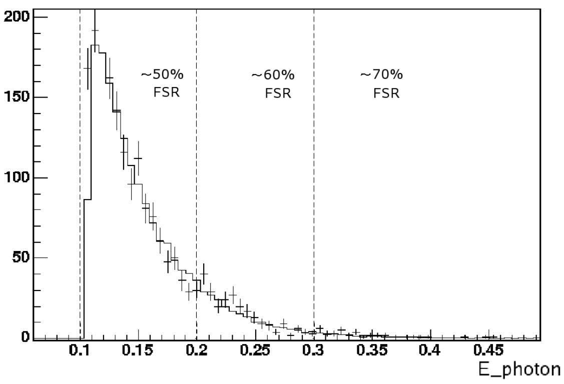

(b)

Fig. 14. (a) Distributions of the parameter M^2 for events of the processes $e^+e^- \to \pi^+\pi^-\gamma$, $e^+e^- \to \mu^+\mu^-\gamma$ and $e^+e^- \to e^+e^-\gamma$ for a c.m.-energy of 780 MeV.

Fig. 15. (b) Distribution of the events $\pi^+\pi^-\gamma$ vs photon energy in relative units. The fraction of the $\pi^+\pi^-\gamma$ events with final state radiation is stated for each vertical zone.

4.3.2 Study of the process $e^+e^- \to \pi^+\pi^-\gamma$ with FSR with KLOE detector

As has been explained in Sec. 4.2, the forward-backward asymmetry

$$\mathcal{A}_{FB}(Q^2) = \frac{N(\theta_{\pi^+} > 90°) - N(\theta_{\pi^+} < 90°)}{N(\theta_{\pi^+} > 90°) + N(\theta_{\pi^+} < 90°)}\,(Q^2) \quad (92)$$

can be used to test the validity of the description of the various mechanisms of the $\pi^+\pi^-$ final state photon emission by confronting the output of the Monte Carlo generator with data. In the following studies, the Monte Carlo generator PHOKHARA6.1 [153] was used. The parameters for the pion form factor were taken from [157] based on the parametrization of Kühn and Santamaria [158]. The parameters for the description of the ϕ direct decay and the double resonance contribution were taken from the KLOE analysis of the neutral mode [154].

To suppress higher order effects, for which the interference and thus the asymmetry is not implemented in the Monte Carlo generator, a rather tight cut on the track mass variable (see Sec. 4.4.1 and Fig. 23) of $|M_{\rm trk} - M_{\pi^\pm}| <$ 10 MeV has been applied in the data in addition to the *large angle* selection cuts described in Sec. 4.4.1. This should reduce events with more than one hard photon emitted and enhance the contribution of the final state radiation processes under study over the dominant ISR process.

The data sets used in the analysis were taken in two different periods:

- The data taken in 2002 was taken with DAΦNE operating at the ϕ-peak, at $\sqrt{s} = M_\phi$ (240 pb^{-1})
- The data taken in 2006 was collected with DAΦNE operating 20 MeV *below* the ϕ-peak, at $\sqrt{s} = 1000$ MeV (230 pb^{-1})

Since the 2006 data were taken more than $4\Gamma_\phi$ below the resonant peak ($\Gamma_\phi = 4.26$ MeV), one expects the contributions from the ϕ direct decay and the double resonance contribution to be suppressed compared to the data taken on the peak in 2002 (see Fig. 10). In fact, one observes a very different shape of the forward-backward asymmetry for the two different data sets, as can be seen in Fig. 16 and Fig. 17. Especially in the region below 0.4 GeV^2 and in the vicinity of the $f_0(980)$ at 0.96 GeV^2 one observes different trends in the asymmetries for the two data sets.

One can also see that qualitatively, the theoretical description used to model the different FSR contributions agrees well with the data, although especially at low $M^2_{\pi\pi}$ the data statistics becomes poor and the data asymmetry points have large errors. In particular, the *off-peak* data in Fig. 17 shows very good agreement above 0.35 GeV^2. In this case, the asymmetry is dominated fully by the bremsstrahlungs-process, as the other processes do not contribute outside the ϕ-resonance. The assumption of pointlike pions (sQED) used to describe the bremsstrahlung in the Monte Carlo generator seems to be valid above 0.35 GeV^2, while below it is difficult to make a statement due to the large statistical errors of the data points.

However, to obtain a solid quantitative statement on the validity of the models, as it is needed e.g. in the radiative return analyses at the KLOE experiment, one needs to understand how a discrepancy between theory and data in the forward-backward asymmetry affects the cross section, as it is the cross section one wants to measure. This requires further work which at the moment is still in progress.

It should also be mentioned that the KLOE experiment has taken almost 10 times more data in the years 2004-2005 than is shown in Fig. 16, with DAΦNE operating at the ϕ-peak energy. This is unfortunately not the case for the *off-peak* data, which is restricted to the dataset shown in Fig. 17. In future, the larger dataset from 2004-2005 may be used to determine with high precision the parameters of the ϕ direct decay and the double resonance contribution, together with the results from the neutral channel and the assumption of isospin symmetry.

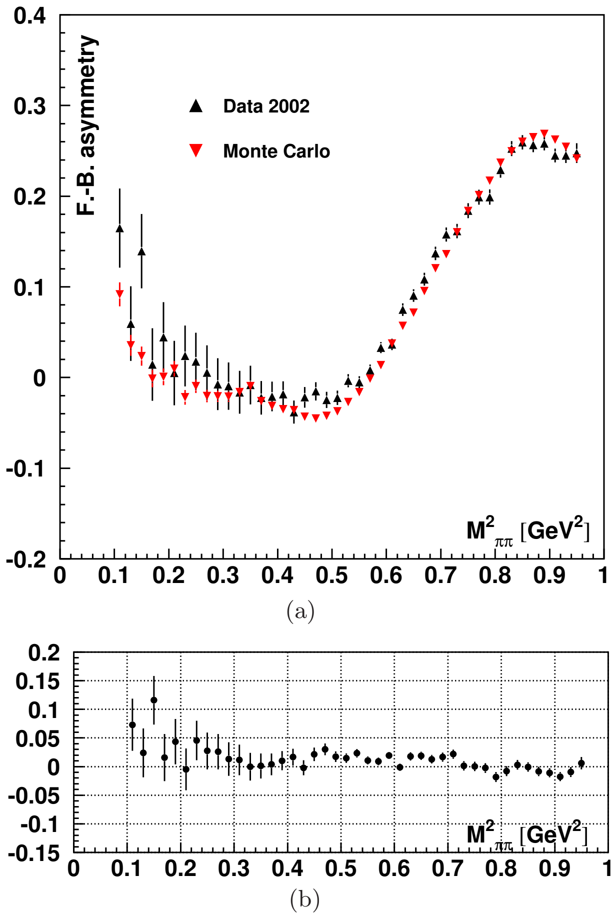

Fig. 16. (a) Forward-Backward asymmetry for data taken at $\sqrt{s} = M_\phi$ in 2002, and the corresponding Monte Carlo prediction using the PHOKHARA 6.1 generator. (b) Absolute difference between the asymmetries from data and Monte Carlo prediction.

4.4 The use of the radiative return as an experimental tool

4.4.1 Radiative return at KLOE

The KLOE experiment, in operation at the DAΦNE e^+e^- collider in Frascati between 1999 and 2006, utilizes the radiative return to obtain precise measurements of hadronic cross sections in the energy range below 1 GeV. As the DAΦNE machine was designed to operate as a meson factory with collision energy equal to the mass of the ϕ-meson ($m_\phi = 1.01946$ GeV), with limited possibility to change the energy of the colliding beams while maintaining stable running conditions, the use of events with initial state radiation of hard photons from the e^+ or the e^- is the only way to access energies below DAΦNE's nominal collision energy. These low-energy cross sections are important in the theoretical evaluation of the muon magnetic moment anomaly $a_\mu = (g_\mu - 2)/2$ [159], and high precision is needed since the uncertainty on the cross section data enters the uncertainty of the theoretical prediction. The channel $e^+e^- \to \pi^+\pi^-$ gives the largest contribution to the hadronic part a_μ^{had} of the anomaly, therefore so far KLOE efforts have concentrated on the derivation of the pion pair-production cross section $\sigma_{\pi\pi}$ from measurements of the differential cross section $\frac{d\sigma_{\pi\pi\gamma(\gamma)}}{dM^2_{\pi\pi}}$, in which $M^2_{\pi\pi}$ is the invariant mass squared of the di-pion system in the final state.

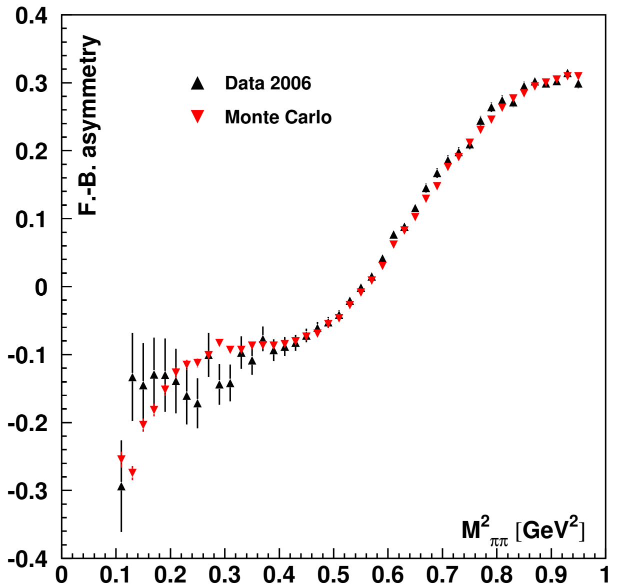

(a)

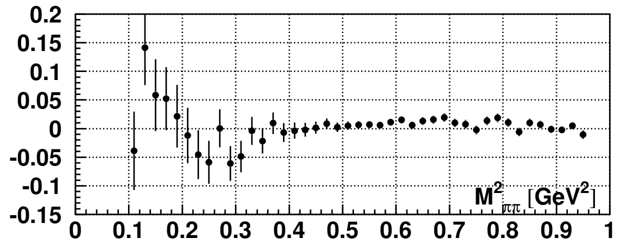

(b)

Fig. 17. (a)Forward-Backward asymmetry for data taken at $\sqrt{s} \simeq 1000$ MeV in 2006, and the corresponding Monte Carlo prediction using the PHOKHARA 6.1 generator. (b) Absolute difference between the asymmetries from data and Monte Carlo prediction.

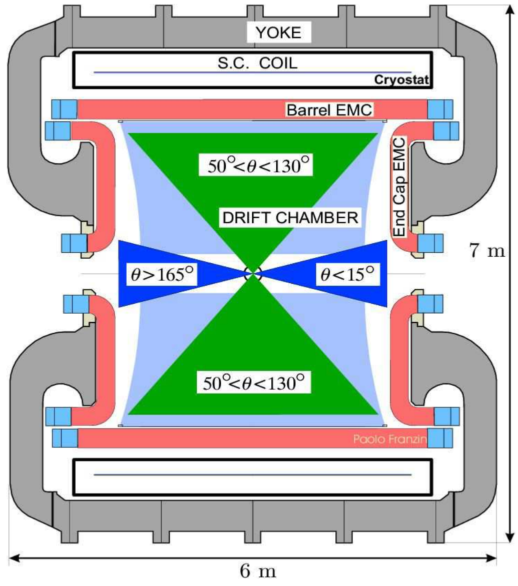

Fig. 18. KLOE detector with the selection regions for small angle photons (narrow cones) and for pion tracks and large angle photons (wide cones).

The KLOE detector (shown in Fig. 18), which consists of a high resolution drift chamber ($\sigma_p/p \leq 0.4\%$) and an electromagnetic calorimeter with excellent time ($\sigma_t \sim 54$ ps$/\sqrt{E\ [\mathrm{GeV}]}$ $\oplus 100$ ps) and good energy ($\sigma_E/E \sim 5.7\%/\sqrt{E\ [\mathrm{GeV}]}$) resolution, is optimally suited for this kind of analyses.

The KLOE $\pi\pi\gamma$ analyses

The KLOE analyses to obtain $\sigma_{\pi\pi}$ use two different sets of acceptance cuts:

- In the *small angle* analysis, photons are emitted within a cone of $\theta_\gamma < 15°$ around the beamline (narrow cones in Fig. 18), and the two charged pion tracks have $50° < \theta_\pi < 130°$. The photon is not explicitly detected, its direction is reconstructed from the track momenta by closing kinematics: $\boldsymbol{p}_\gamma \simeq \boldsymbol{p}_{miss} = -(\boldsymbol{p}_{\pi^+} + \boldsymbol{p}_{\pi^-})$. The separation of pion- and photon selection regions in this analysis greatly reduces the contamination from the resonant process $e^+e^- \to \phi \to \pi^+\pi^-\pi^0$ in which the π^0 mimicks the missing momentum of the photon(s) and from the final state radiation process $e^+e^- \to \pi^+\pi^-\gamma_{\mathrm{FSR}}$. Since ISR-photons are mostly collinear with the beam line, a high statistics for the ISR signal events remains. On the other hand, a high energy photon emitted at angles close to the incoming beams forces the pions also to have a small angle with respect to the beamline (and thus outside the selection cuts), resulting in a kinematical suppression of events with $M^2_{\pi\pi} < 0.35$ GeV^2.
- The *large angle* analysis requires both photons and pions to be emitted at $50° < \theta_{\pi,\gamma} < 130°$ (wide cones in Fig. 18), allowing for a detection of the photons in the barrel of the calorimeter. This analysis allows to reach the 2π threshold region, at the price of higher background contributions from the $\pi^+\pi^-\pi^0$ final state and events with final state radiation. In addition, events from the decays $\phi \to f_0\gamma \to \pi^+\pi^-\gamma$ and $\phi \to \pi^\pm\rho^\mp \to \pi^\pm\pi^\mp\gamma$, which need to be described by model-dependent parameterisations, contribute to the spectrum of selected events (running at ϕ peak).

Two analyses based on the *small angle* acceptance cuts have been carried out. The first one using 140 pb^{-1} of data taken in the year 2001 was published in 2005 [67], the second one, based on 240 pb^{-1} of data taken in 2002 was published in 2008 [160].

The differential cross section is obtained from the spectrum of selected events N^{sel} subtracting the residual background (mostly $\mu\mu\gamma(\gamma)$, $\pi\pi\pi$ and radiative Bhabha events) and dividing by the selection efficiencies and the integrated luminosity:

$$\frac{d\sigma_{\pi\pi\gamma(\gamma)}}{dM^2_{\pi\pi}} = \frac{N^{\mathrm{sel}} - N^{\mathrm{bkg}}}{\Delta M^2_{\pi\pi}} \cdot \frac{1}{\varepsilon_{\mathrm{sel}}} \cdot \frac{1}{\int L dt} \qquad (93)$$

$\Delta M^2_{\pi\pi}$ is the bin width used in the analysis (typically 0.01 GeV^2), and $\int L dt$ is the integrated luminosity obtained from Bhabha events detected at large angles ($55° < \theta_e < 125°$) and the reference cross section from the BABAYAGA generator [161,162] (discussed in Sec. 2). The total cross section is then obtained from the formula

$$\sigma_{\pi\pi}(M^2_{\pi\pi}) = s \cdot \frac{d\sigma_{\pi\pi\gamma(\gamma)}}{dM^2_{\pi\pi}} \frac{1}{H(s, M^2_{\pi\pi})} \tag{94}$$

In this formula, s is the squared energy at which the DAΦNE collider is operated during the data taking, and $H(s, M^2_{\pi\pi})$ is the radiator function describing the emission of photons from the e^+ or the e^- in the initial state. Note that Eq. 94 does not contain the effects from final state radiation from pions. These effects complicate the analysis, since the KLOE detector can not distinguish whether photons in an event were emitted in the initial or the final state. The PHOKHARA Monte Carlo generator [29], which includes final state radiation at next-to-leading order in the pointlike-pion approximation, is used to properly take into account final state radiation in the analyses. This is important because the *bare* cross section used to evaluate $a_\mu^{\rm had}$ via an appropriate dispersion integral should be inclusive with respect to final state radiation, and also needs to be undressed from vacuum polarisation effects present in the virtual photon produced in the e^+e^- annihilation. For the latter, we use a function provided by F. Jegerlehner [163] (see Section 5), and correct the cross section via

$$\sigma^{\rm bare}_{\pi\pi}(M^2_{\pi\pi}) = \sigma^{dressed}_{\pi\pi}(M^2_{\pi\pi}) \left(\frac{\alpha(0)}{\alpha(M^2_{\pi\pi})}\right)^2 \tag{95}$$

Here $\alpha(0)$ is the fine structure constant in the limit $q = 0$, and $\alpha(M^2_{\pi\pi})$ represents its effective value at the specific value of the squared invariant mass of the di-pion system. Since the hadronic contribution to $\alpha(M^2_{\pi\pi})$ comes from a dispersion integral which includes the hadronic cross section itself as the integrand (see Sec. 5), the correct procedure has to be iterative and it should include the same data that must be corrected. However, since the correction is at the few percent level, the inclusion of the new KLOE data will not change $\alpha(M^2_{\pi\pi})$ at a level which would significantly affect the analyses. We therefore have used the values for $\alpha(M^2_{\pi\pi})$ derived from the existing hadronic cross section database. As an example, Fig. 19 shows the KLOE result for $d\sigma_{\pi\pi\gamma(\gamma)}/dM^2_{\pi\pi}$ obtained from data taken in the year 2002 [160]. Inserting this differential cross section into Eq. 94 and the outcome into Eq. 95, one derives $\sigma^{bare}_{\pi\pi}$. Using the *bare* cross section to get the $\pi\pi$-contribution to $a_\mu^{\rm had}$ between 0.35 and 0.95 GeV^2 then gives the value (in units of 10^{-10})

$$a_\mu^{\pi\pi}(0.35 - 0.95\text{GeV}^2) = (387.2 \pm 0.5_{\rm stat} \pm 2.4_{\rm exp} \pm 2.3_{\rm th})$$

Table 1 shows the contributions to the systematic errors on $a_\mu^{\pi\pi}(0.35 - 0.95\ \text{GeV}^2)$.

Radiative corrections and Monte Carlo tools

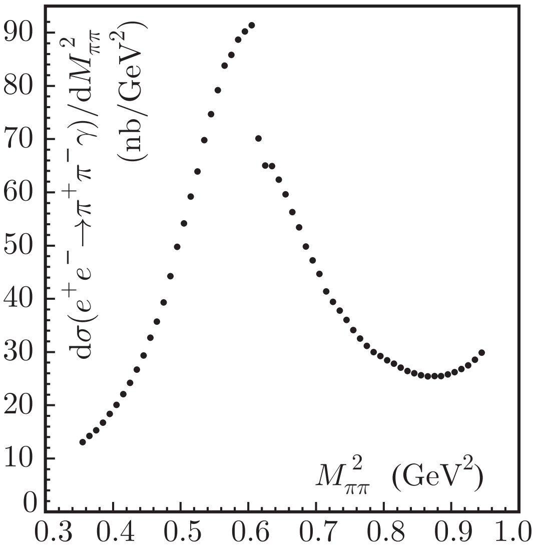

Fig. 19. Differential radiative cross section $d\sigma_{\pi\pi\gamma(\gamma)}/dM^2_{\pi\pi}$, inclusive in θ_π and with $0^o < \theta_\gamma < 15^o$ or $165^o < \theta_\gamma < 180^o$ measured by the KLOE experiment [160].

Reconstruction Filter	negligible
Background subtraction	0.3 %
Trackmass	0.2 %
Particle ID	negligible
Tracking	0.3 %
Trigger	0.1 %
Unfolding	negligible
Acceptance ($\theta_{\pi\pi}$)	0.2 %
Acceptance (θ_π)	negligible
Software Trigger (L3)	0.1 %
Luminosity ($0.1_{th} \oplus 0.3_{exp}$)%	0.3 %
$\sqrt{s}$ dep. of H	0.2 %
Total exp systematics	0.6 %
Vacuum Polarization	0.1 %
FSR resummation	0.3 %
Rad. function H	0.5 %
Total theory systematics	0.6 %

Table 1. List of systematic errors on the $\pi\pi$-contribution to a_μ^{had} between 0.35 and 0.95 GeV^2 when using the $\sigma_{\pi\pi}$ cross section measured by the KLOE experiment in the corresponding dispersion integral [160].

The radiator function is a crucial ingredient in this kind of radiative return analyses, it is obtained using the relation

$$H(s, M^2_{\pi\pi}) = s \cdot \frac{3M^2_{\pi\pi}}{\pi\alpha^2\beta^3_\pi} \cdot \left.\frac{d\sigma^{\rm ISR}_{\pi\pi\gamma(\gamma)}}{dM^2_{\pi\pi}}\right|_{|F_{2\pi}|^2=1}, \tag{96}$$

in which $\left.\frac{d\sigma^{ISR}_{\pi\pi\gamma(\gamma)}}{dM^2_{\pi\pi}}\right|_{|F_{2\pi}|^2=1}$ is evaluated using the PHOKHARA Monte Carlo generator in next-to-leading order ISR-only configuration, with the squared pion form factor $|F_{2\pi}|^2$ set to 1. $\beta_\pi = \sqrt{1 - \frac{4m^2_\pi}{M^2_{\pi\pi}}}$ is the pion velocity. While

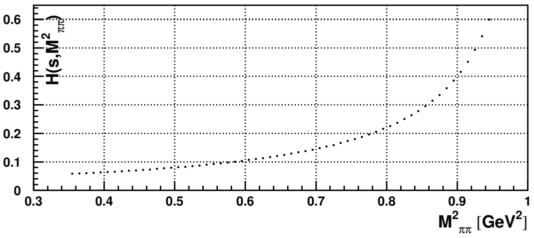

Fig. 20. The dimensionless radiator function $H(s, M^2_{\pi\pi})$, inclusive in $\theta_{\pi,\gamma}$. The value used for s in the Monte Carlo production was $s = (M_\phi)^2 = (1.019456\ \mathrm{GeV})^2$.

Eq. 96 provides a convenient mechanism to extract the dimensionless quantity $H(s, M^2_{\pi\pi})$ also for specific angular regions of pions and photons by applying the relevant cuts to $\left.\frac{d\sigma^{ISR}_{\pi\pi\gamma(\gamma)}}{dM^2_{\pi\pi}}\right|_{|F_{2\pi}|^2=1}$, in the published KLOE analyses, $H(s, M^2_{\pi\pi})$ is evaluated fully inclusive for pion and photon angles: $0^\circ < \theta_{\pi,\gamma} < 180^\circ$. Fig. 20 shows the radiator function in the range of $0.35 < M^2_{\pi\pi} < 0.95\ \mathrm{GeV}^2$. As can be seen from Table 1, the 0.5% uncertainty of the radiator function quoted by the authors of PHOKHARA translates into an uncertainty of 0.5% in the $\pi\pi$-contribution to a_μ^{had} between 0.35 and 0.95 GeV^2, giving the largest individual contribution and dominating the theoretical systematic error.

The presence of events with final state radiation in the data sample affects the analyses in several ways:

- Passing from $M^2_{\pi\pi}$ to $(M^0_{\pi\pi})^2$ The presence of final state radiation shifts the observed value of $M^2_{\pi\pi}$ (evaluated from the momenta of the two charged pion tracks in the events) away from the value of the invariant mass squared of the virtual photon produced in the collision of the electron and the positron, $(M^0_{\pi\pi})^2$. The transition from $M^2_{\pi\pi}$ to $(M^0_{\pi\pi})^2$ is performed using a modified version of the PHOKHARA Monte Carlo generator, which allows to (approximately) determine whether a generated photon comes from the initial or the final state [164]. Fig. 21 shows the probability matrix relating $M^2_{\pi\pi}$ to $(M^0_{\pi\pi})^2$ by giving the probability for an event in a bin of $M^2_{\pi\pi}$ to end up in a bin of $(M^0_{\pi\pi})^2$. It can be seen that the shift is only in one direction, $(M^0_{\pi\pi})^2 \geq M^2_{\pi\pi}$, so events with one photon from initial state radiation and one photon from final state radiation move to a higher value of $(M^0_{\pi\pi})^2$. The entries lining up above $(M^0_{\pi\pi})^2 \simeq 1.03\ \mathrm{GeV}^2$ represent events with two pions and only one photon, emitted in the final state. Events of this type have $(M^0_{\pi\pi})^2 = s$, there is no hard photon from initial state radiation present. Since in the KLOE analyses, the maximum value of $(M^0_{\pi\pi})^2$ for which the cross sections are measured ($0.95\ \mathrm{GeV}^2$) is sufficiently smaller than $s \simeq M^2_\phi$ of the DAΦNE collider, these *leading-order* final state radiation events need to be taken out in the analysis. By moving these events to $(M^0_{\pi\pi})^2 = s$, the passage from $M^2_{\pi\pi}$ to $(M^0_{\pi\pi})^2$ automatically performs this task.

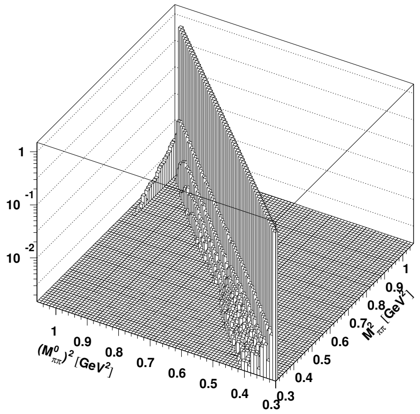

Fig. 21. Probability matrix relating the measured quantity $M^2_{\pi\pi}$ to $(M^0_{\pi\pi})^2$. To produce this plot, a private version of the PHOKHARA Monte Carlo generator was used [164]. The photon angle is restricted to $\theta_\gamma < 15^\circ$ ($\theta_\gamma > 165^\circ$).

Fig. 22 shows the fraction of events from *leading-order* final state radiation contributing to the total number of events, evaluated with the PHOKHARA event generator. Since in the *small angle* analysis the angular regions for pions and photons are separated, final state radiation, for which the photons are emitted preferably along the direction of the pions, is suppressed to less than 0.5%. Using *large angle* acceptance cuts, the effect is much bigger, especially above and below the ϱ-resonance, where it can reach 20-30%. The correction of the shift in $M^2_{\pi\pi}$ depends on the implementation of final state radiation in the Monte Carlo generator in terms of model dependence and missing contributions. It also relies on the correct assignment of photons coming from the initial or the final state, however, in case of symmetrical cuts in θ_γ, interference effects between the two states vanish and the separation of initial and final state amplitudes is feasible.
- The acceptance in θ_γ. Since the direction of the photons emitted in the final state is peaked along the direction of the pions, and the photons are emitted in the initial state along the e^+/e^- direction, the choice of the acceptance cuts affects the amount of final state radiation in the analyses. Using the *small angle* analysis cuts, a large part of final state radiation is suppressed by the separation of the pion and photon acceptance regions, and consequently needs to be reintroduced using corrections obtained from Monte Carlo simulations to arrive at a result which is inclusive with respect to final state radiation (as needed in the dispersion integral for $a_\mu^{\pi\pi}$). Even if in the *large angle* analysis the fraction of events with final state radiation surviving the selection is larger, again the missing part has to be added using Monte Carlo simulations. The acceptance correction for the cut in θ_γ is evaluated for initial and final state radiation using the PHOKHARA generator, and the small differences found in the comparison of data and Monte Carlo distributions contribute to the

systematic uncertainty of the measurement (see Table 1 and [165]).

- The distributions of kinematical variables. Cuts on the kinematical *trackmass* variable M_{trk} (see eq. 86), introduced in the analyses to remove background from the process $e^+e^- \to \phi \to \pi^+\pi^-\pi^0$, take out also a fraction of the events with final state radiation, necessitating a correction to obtain an inclusive result. Fig. 23 shows the effect final state radiation has on the distribution of the trackmass variable. The radiative tail of multi-photon events to the right of the peak at the $\pi^\pm$ mass increases because the additional radiation moves events from the peak to higher values in M_{trk}. The width of the peak at $M_{\pi^\pm}$ is due to the detector resolution, the plot was produced using the PHOKHARA event generator interfaced with the KLOE detector simulation [166]. Between 150 and 200 MeV, a $M^2_{\pi\pi}$-dependent cut is used in the event selection to reject the $\pi^+\pi^-\pi^0$ events which have a value of $M_{\mathrm{trk}} > M_{\pi^\pm}$. In this region, the cut also acts on the signal events. Missing terms concerning final state radiation in the Monte Carlo simulation or the non-validity of the pointlike-pion approximation used in PHOKHARA may affect the shape of the radiative tail in the trackmass variable. To overcome this, in the KLOE analyses, small corrections are applied to the momenta and the angles of the charged particles in the event in the simulation to obtain good agreement in the shape of M_{trk} for Monte Carlo simulation and data [165].
- The division by the radiator function $H(s, M^2_{\pi\pi})$. In this case, one assumes perfect factorization between the ISR and the FSR process. This has been tested by performing the analysis in an inclusive and exclusive approach with respect to final state radiation, the assumption was found to be valid within 0.2% [67,167].

It has been argued that contributions from events with two hard photons in the final state, which are not included in the PHOKHARA generator, may have an effect on the analyses [75].

The effect of the direct decay $\phi \to \pi^+\pi^-\gamma$ on the radiative return analysis has been already addressed in [41]. Running at $\sqrt{s} \simeq 1.02$ GeV, the amplitude for the processes $\phi \to (f_0(980) + f_0(600))\gamma \to \pi^+\pi^-\gamma$ interferes with the amplitude for the final state radiation process. Due to the yet unclear nature of the scalar states $f_0(980)$ and $f_0(600)$, the effect on the $\pi^+\pi^-\gamma(\gamma)$ cross section depends on the model used to describe the scalar mesons. The possibility to simulate ϕ decays together with the processes for initial and final state radiation has been implemented in the PHOKHARA event generator in [31], using two characteristic models for the ϕ decays: the "no structure" model of [168] and the K^+K^- loop model of [169]. A refined version of the K^+K^- loop model [152] and the double vector resonance $\phi \to \pi^\pm\varrho^\mp(\to \pi^\mp\gamma)$ have been included as described in [44]. Using parameter values for the different ϕ decays found in the analysis of the neutral channel $\phi \to (f_0(980) + f_0(600))\gamma \to \pi^0\pi^0\gamma$ [152,154], one can estimate the effect on the different analyses. While in the *small angle* analysis, there is no significant effect due to the choice of the acceptance cuts, in the *large angle* selection, the effect is of the order of several percent, and can reach up to 20% in the vicinity of the $f_0(980)$, as shown in Fig. 24, (a). While this allows to study the different models for the direct decays of ϕ-mesons (see also Sec. 4.3.2), it prevents a precise measurement of $\sigma_{\pi\pi}$ until

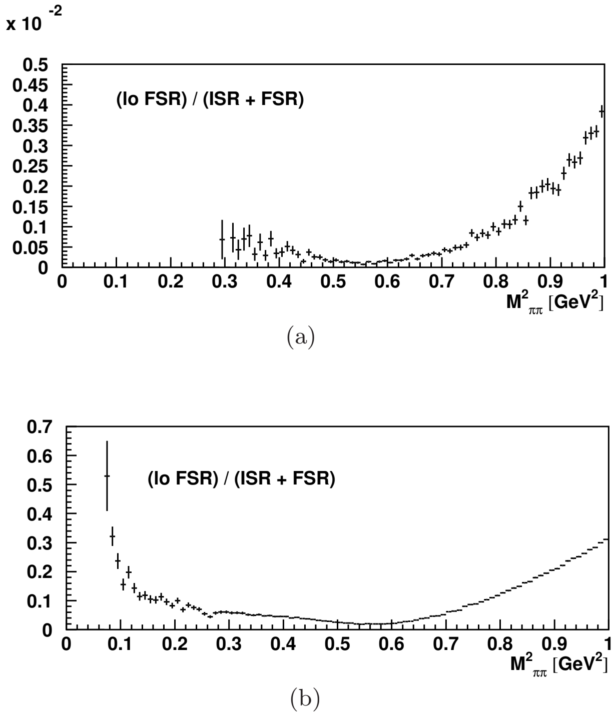

Fig. 22. (a) Fraction of events with leading order final state radiation in the *small angle* selection: $50^\circ < \theta_\pi < 130^\circ$ and $\theta_\gamma < 15^\circ$ ($\theta_\gamma > 165^\circ$). (b) Fraction of events with leading order final state radiation in the *large angle* selection: $50^\circ < \theta_\pi < 130^\circ$ and $50^\circ < \theta_\gamma < 130^\circ$. The PHOKHARA generator was used to produce the plots.

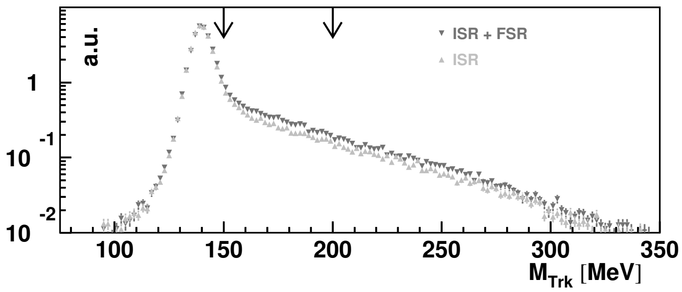

Fig. 23. Modification of the distribution of the trackmass variable due to the presence of final state radiation (dark grey triangles) compared to the one with initial state radiation only (light grey triangles). The arrows indicate the region in which the $M^2_{\pi\pi}$-dependent cut is applied in the analysis. The plot was created with the PHOKHARA generator interfaced to the KLOE detector simulation [166].

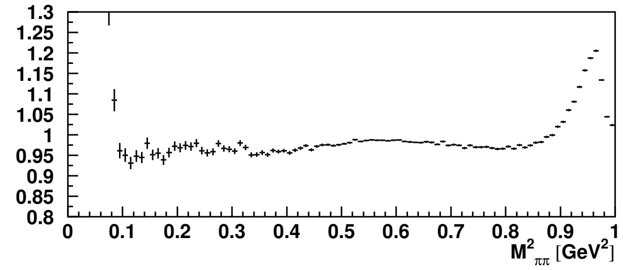

(a)

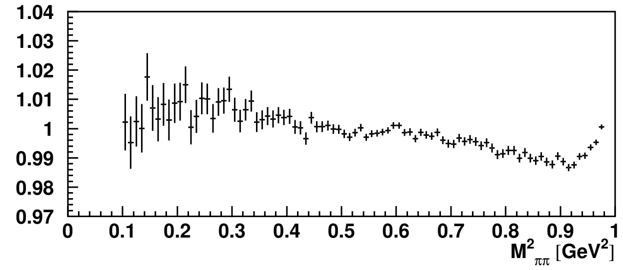

(b)

Fig. 24. (a): $d\sigma_{\pi\pi\gamma}^{(ISR+FSR+f_0+\varrho\pi)}/d\sigma_{\pi\pi\gamma}^{(ISR+FSR)}$ for $\sqrt{s} = 1.019$ GeV. (b): $d\sigma_{\pi\pi\gamma}^{(\mathrm{ISR}+FSR+f_0+\varrho\pi)})/d\sigma_{\pi\pi\gamma}^{(\mathrm{ISR}+FSR)}$ for $\sqrt{s} = 1$ GeV. Both plots were produced with the PHOKHARA 6.1 event generator using *large angle* acceptance regions for pions and photons, with model parameters for the f_0 and $\varrho\pi$ contributions found in [152,154].

the model and the parameters are understood with better uncertainty. An obvious way out is to use data taken at a value of $\sqrt{s}$ outside the narrow peak of the ϕ resonance ($\Gamma_\phi = 4.26 \pm 0.04$ MeV [1]). In 2006, the KLOE experiment has taken ~ 250 pb^{-1} of data at $\sqrt{s} = 1$ GeV, 20 MeV below M_ϕ. As can be seen in Fig. 24 (b), this reduces the effect due to contributions from $f_0\gamma$ and $\varrho\pi$ decays of the ϕ-meson to within $\pm 1\%$.

Normalization with muon events

An alternative method to extract the pion form factor is to normalize the differential cross section $d\sigma_{\pi\pi\gamma(\gamma)}/dM^2_{\pi\pi}$ directly to the process $e^+e^- \to \mu^+\mu^-\gamma(\gamma)$, $d\sigma_{\mu\mu\gamma(\gamma)}/dM^2_{\mu\mu}$, in each bin of $\Delta M^2_{\pi\pi} = \Delta M^2_{\mu\mu}$. Radiative corrections like the effect of vacuum polarisation, the radiator function and also the integrated luminosity $\int Ldt$ cancel out in the ratio of pions over muons, only the effects from final state radiation (which is different for pions and muons) need to be taken into account consistently. An approach currently under way at KLOE uses the following equation to obtain $|F_{2\pi}|^2$:

$$|F_{2\pi}(s')|^2 \cdot (1+\eta(s')) = \frac{4(1+2m_\mu^2/s')\beta_\mu}{\beta_\pi^3} \cdot \frac{(\frac{d\sigma_{\pi\pi\gamma(\gamma)}}{dM^2_{\pi\pi}})^{\mathrm{ISR}+FSR}}{(\frac{d\sigma_{\mu\mu\gamma(\gamma)}}{dM^2_{\mu\mu}})^{\mathrm{ISR}}} \tag{97}$$

In this formula, the measured differential cross section $d\sigma_{\pi\pi\gamma(\gamma)}/dM^2_{\pi\pi}$ should be inclusive with respect to pionic final state radiation, while the measured cross section $d\sigma_{\mu\mu\gamma(\gamma)}/dM^2_{\mu\mu}$ should be exclusive for muonic final state radiation. $s' = M^2_{\pi\pi} = M^2_{\mu\mu}$ is the squared invariant mass of the di-pion or the di-muon system after the respective corrections concerning final state radiation. Using this approach one gets on the left-hand side the pion form factor times the factor $(1+\eta(s'))$, which describes the effect of the pionic final state radiation. This *bare* form factor is the quantity needed in the dispersion integral for the $\pi\pi$-contribution to a_μ^{had}. While the measurement of $d\sigma_{\pi\pi\gamma(\gamma)}/dM^2_{\pi\pi}$ and its corrections for pionic final state radiation are very similar to the one using the normalization with Bhabha events already performed at KLOE, the corrections needed to subtract the muonic final state radiation from the $d\sigma_{\mu\mu\gamma(\gamma)}/dM^2_{\mu\mu}$ cross section are pure QED and can be obtained from the PHOKHARA generator, which includes final state radiation for muon pair production at next-to-leading order [30]. Due to the fact that the KLOE detector does not provide particle IDs, pions and muons have to be separated and identified using kinematical variables (e.g. the aforementioned trackmass variable) [61]. The analysis is in progress and a systematic precision similar to the one obtained in the absolute measurement is expected.

4.4.2 Radiative return at BABAR

The BABAR radiative return program aims for the study of all significant hadronic processes in electron-positron annihilation $e^+e^- \to$ hadrons for energies from threshold to about 4.5 GeV. Moreover, hadron spectroscopy of the initial $\mathrm{J}^{PC} = 1^{--}$ states, which are produced in e^+e^- collision, and of their decay products is performed. In this chapter BABAR results for processes with 3, 4, 5 and 6 hadrons in the final state, as well as measurements of baryon form factors in the timelike region are reported. A precision analysis of the pion form factor, i.e. of the cross section $e^+e^- \to \pi^+\pi^-$, which is essential for an improved determination of the hadronic contrubution to the anomalous magnetic moment of the muon, is underway. The results presented in this chapter are based on a total integrated luminosity of 230 fb^{-1}, except for the 3π and four-hadrons channels of Ref. [102], which were analyzed using a data sample of 90 fb^{-1}. The total BABAR data sample collected between the years 1999 to 2008 amounts to be 530 fb^{-1}. A typical feature common to all radiative return analyses at BABAR is a wide coverage of the entire mass range of interest in one single experiment with reduced point-by-point uncertainties compared to previous experiments.

$e^+e^- \to 3$ Pions

The $\pi^+\pi^-\pi^0$ mass spectrum has been measured from 1.05 GeV up to the J/ψ mass region with a systematic error of $\sim 5\%$ below 2.5 GeV and up to $\sim 20\%$ at higher masses [101]. The spectrum is dominated by the ω, ϕ and J/ψ resonances. The BABAR measurement could improve significantly on the world knowledge of the excited ω states. The spectrum has been fitted up to 1.8 GeV and the following results for the masses and widths of the ω'

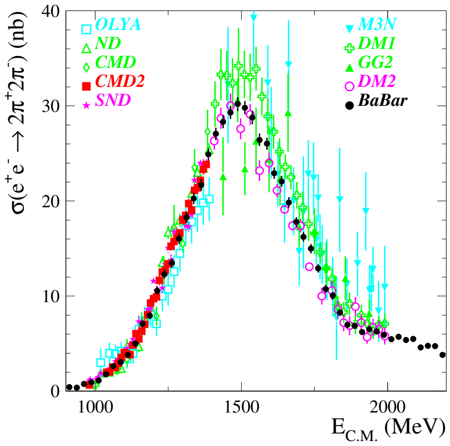

Fig. 25. BABAR measurement of the energy dependence of the $e^+e^- \to \pi^+\pi^-\pi^+\pi^-$ cross section obtaied by radiative return in comparison with the world data set.

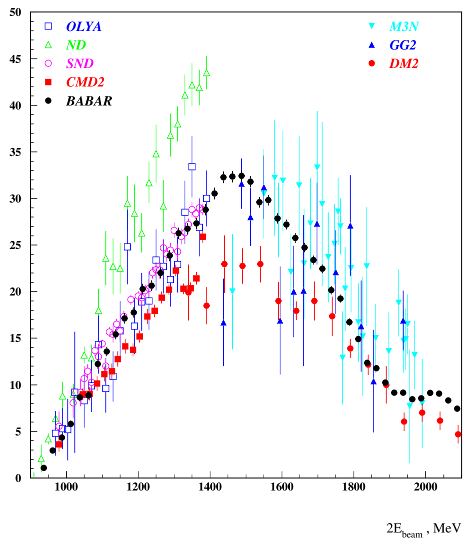

Fig. 26. Preliminary BABAR data for the $e^+e^- \to \pi^+\pi^-\pi^0\pi^0$ cross section in comparison with previous experiments.

and ω'' states have been found: $M(\omega') = (1350 \pm 20 \pm 20)$ MeV, $\Gamma(\omega') = (450 \pm 70 \pm 70)$ MeV, $M(\omega'') = (1660 \pm 10 \pm 2)$ MeV, $\Gamma(\omega'') = (230 \pm 30 \pm 20)$ MeV.

$e^+e^- \to 4$ *Hadrons*

The $\pi^+\pi^-\pi^+\pi^-$, $K^+K^-\pi^+\pi^-$ and $K^+K^-K^+K^-$ exclusive final states have been measured from theshold up to 4.5 GeV with systematic errors of 5%, 15% and 25%, respectively [102]. The $K^+K^-K^+K^-$ measurement is the first measurement of this process ever. Fig. 25 shows the mass distribution of the $\pi^+\pi^-\pi^+\pi^-$ channel. We identify the typical feature common to all radiative return analyses at BABAR, namely a wide coverage of mass range in one single experiment with reduced point-by-point uncertainties. Background is relatively low for all channels under study (e.g. a few percent at 1.5 GeV for $\pi^+\pi^-\pi^+\pi^-$) and is dominated by ISR-events of higher multiplicities and of continuum non-ISR events at higher masses. The $\pi^+\pi^-\pi^+\pi^-$ final state is dominated by the two-body intermediate state $a_1(1260)\pi$; the $K^+K^-\pi^+\pi^-$ final state shows no significant two-body states, but rich three-body structure, including $K^*(890)K\pi$, $\phi\pi\pi$, $K_2^*(1430)K\pi$ and ρKK.

Fig. 26 shows BABAR preliminary results for the process $e^+e^- \to \pi^+\pi^-\pi^0\pi^0$. The current systematic error of the measurement varies from 8% around the peak of the cross section to 14% at 4.5 GeV. BABAR results are in agreement with SND [170] in the energy range below 1.4 GeV and show a huge improvement for higher energies (> 1.4 GeV). In the energy range above 2.5 GeV this is the first measurement ever. The $e^+e^- \to \pi^+\pi^-\pi^0\pi^0$ final state is dominated by the $\omega\pi^0$, $a_1(1260)\pi$ and $\rho^+\rho^-$ intermediate channels, where the latter channel has been observed for the first time.

A specific analysis was devoted to the intermediate structures in the $e^+e^- \to K^+K^-\pi^+\pi^-$ and $e^+e^- \to K^+K^-\pi^0\pi^0$ channels [106]. Of special interest is the intermediate state $\phi f_0(980)$, where the decays $f_0(980) \to \pi^+\pi^-$ and $f_0(980) \to \pi^0\pi^0$ have been looked at. A peak is observed in the $\phi f_0(980)$ channel at a mass $M = 2175 \pm 18$ MeV and a width $\Gamma = 58 \pm 2$. The new state is usually denoted as Y(2175) and is also clearly visible in the $K^+K^- f_0$ spectrum.

$e^+e^- \to 2(\pi^+\pi^-)\pi^0$, $2(\pi^+\pi^-)\eta$

The $e^+e^- \to 2(\pi^+\pi^-)\pi^0$ cross section has been measured by BABAR from threshold up to 4.5 GeV [108]. A large coupling of the J/ψ and $\psi(2S)$ to this channel is observed. The systematic error of the measurement is about 7% around the peak of the mass spectrum. In the $\pi^+\pi^-\pi^0$ mass distribution the ω and η peaks are observed; the rest of the events have a $3\pi\rho$ structure.

BABAR performed also the first measurement of the $e^+e^- \to 2(\pi^+\pi^-)\eta$ cross section. A peak value of about 1.2 nb at about 2.2 GeV is observed, followed by a monotonic decrease towards higher energies. Three intermediate states are seen: $\eta\rho(1450)$, $\eta'\rho(770)$ and $f_1(1285)\rho(770)$.

$e^+e^- \to 6$ *Hadrons*

The six-hadron final state has been measured in the exclusive channels $3(\pi^+\pi^-)$, $2(\pi^+\pi^-)2\pi^0$ and $K^+K^-2(\pi^+\pi^-)$ [104]. The cross section in the last case has never been measured before; the precision in the first two cases is $\sim 20\%$, which is a large improvement with respect to existing data. Again, the entire energy range from threshold up to 4.5 GeV is measured in one single experiment. The distributions for the final states $3(\pi^+\pi^-)$ and $2(\pi^+\pi^-)2\pi^0$ are shown in Fig. 27. A clear dip is visible at about 1.9 GeV in both pion modes. A similar feature was already seen by FOCUS [171] in the diffractive photo-production of six charged pions. The spectra are fitted by BABAR using the sum of a Breit-Wigner resonance function and a Jacob-Slansky continuum shape. For the $3(\pi^+\pi^-)$ $(2(\pi^+\pi^-)2\pi^0)$ mode, BABAR obtains values of 1880 ± 30 MeV (1860 ± 20 MeV) for the resonance peak, 130 ± 30 MeV (160 ± 20 MeV)

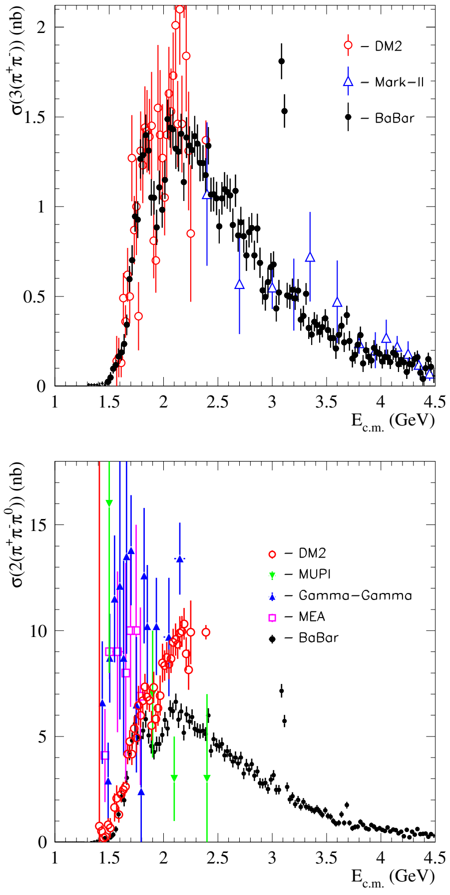

Fig. 27. The energy dependence of the $e^+e^- \to 3(\pi^+\pi^-)$ (upper plot) and the $e^+e^- \to 2(\pi^+\pi^-)2\pi^0$ (lower plot) cross section obtained by BABAR (filled circles) by radiative return in comparison with previous data.

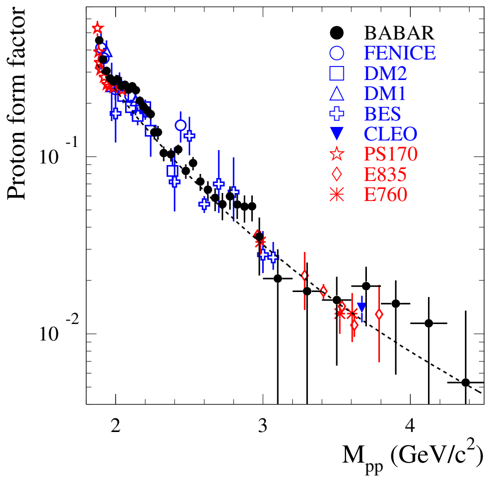

Fig. 28. The $e^+e^- \to p\bar{p}$ cross section measured by BABAR (filled circles) in comparison with data from other e^+e^- colliders (blue points) and from $\bar{p}p$ experiments (red points).

for the resonance width and $21^o \pm 14^o$ ($-3^o \pm 15^o$) for the phase shift between the resonance and continuum.

$e^+e^- \to K^+K^-\pi^0, K^+K^-\eta$, $K_SK^\pm\pi^\mp$
A recent BABAR ISR-analysis is dedicated to three hadrons in the final state, including a pair of kaons ($K^+K^-\pi^0$, $KK_S\pi$); a peak near 1.7 GeV, which is mainly due to the $\phi'(1680)$ state, is observed. A Dalitz plot analysis shows that the $KK^*(892)$ and $KK_2^*(1430)$ intermediate states are dominating the $K\bar{K}\pi$ channel. A fit to the $e^+e^- \to K\bar{K}\pi$ cross section assuming the expected contributions from the $\phi, \phi', \phi'', \rho^0, \rho', \rho''$ states was performed. The parameters of the ϕ' and other excited vector meson states are compatible with the PDG values.

Timelike proton form factor $e^+e^- \to p\bar{p}$, hyperon form factors $e^+e^- \to \Lambda^0\bar{\Lambda}^0, \Lambda^0\bar{\Sigma}^0, \Sigma^0\bar{\Sigma}^0$
BABAR has also performed a measurement of the $e^+e^- \to p\bar{p}$ cross section [103]. This timelike form factor is parameterized by the electric and magnetic formfactor G_E and G_M.

$$\sigma_{e^+e^-\to p\bar{p}}(s) = \frac{4\pi\alpha^2 C}{3s}\sqrt{1-\frac{2m_p^2}{s}} \times (|G_M(s)|^2 + \frac{2m_p^2}{s}|G_E(s)|^2),$$

where the factor C accounts for the Coulomb interaction of the final state particles. The proton helicity angle θ_p in the $p\bar{p}$ rest frame can be used to separate the $|G_E|^2$ and $|G_M|^2$ terms. Their respective variations are approximately $\sim \sin^2\theta_p$ and $\sim (1+\cos^2\theta_p)$. By fitting the $\cos\theta_p$ distribution to a sum of the two terms, the ratio $|G_E|/|G_M|$ can be extracted. This is done separately in six bins of $M_{p\bar{p}}$. The results disagree significantly with previous measurements from LEAR [172] above threshold. BABAR observes a ratio $|G_E|/|G_M| > 1$ above threshold, while at larger values of $M_{p\bar{p}}$ the BABAR measurement finds $|G_E|/|G_M| \approx 1$. LEAR data on the contrary shows a behaviour $|G_E|/|G_M| < 1$ above threshold.
In order to compare the cross section measurement with previous data (e^+e^- and $\bar{p}p$ experiments), the *effective* form factor G is introduced: $G = \sqrt{|G_E|^2 + 2m_p^2/s|G_M|^2}$. The BABAR measurement of G is in good agreement with existing results, as can be seen in Fig. 28. The structure of the form factor is rather complicated; the following observations can be made: (i) BABAR confirms an increase of G towards threshold as seen before by other experiments; (ii) two sharp drops of the spectrum at $M_{p\bar{p}} = 2.25$ and 3.0 GeV are observed; (iii) data at large values $M_{p\bar{p}} > 3$ GeV is in good agreement with the prediction from perturbative QCD.
A continuation of the ISR program with baryon final states is the measurement of the $e^+e^- \to \Lambda\bar{\Lambda}$ cross section [109]. So far only one data point from DM2 [173] was existing for this channel, which is in good agreement with BABAR

data. About 360 $\Lambda\bar{\Lambda}$ events could be selected using the $\Lambda \to p\pi$ decay. In two invariant mass bins an attempt has been made to extract the ratio of the electric to magnetic form factor $|G_E|/|G_M|$. In the mass range below 2.4 GeV this ratio is above unity - as in the proton case - with a significance of one standard deviation ($|G_E|/|G_M| = 1.73^{+0.99}_{-0.57}$). Above 2.4 GeV the ratio is consistent with unity ($|G_E|/|G_M| = 0.71^{+0.66}_{-0.71}$). Also the Λ polarization and the phase between G_E and G_M was studied using the slope of the angle between the polarization axis and the proton momentum in the Λ rest frame. The following limit on Λ polarization is obtained: $-0.22 < \zeta < 0.28$; the relative phase between the two form factors is measured as $-0.76 < \sin(\phi) < 0.98$, which is not yet significant due to limited statistics.

Finally, the first measurements of the $e^+e^- \to \Sigma^0\bar{\Sigma}^0$ and $e^+e^- \to \Sigma^0\bar{\Lambda}(\Lambda\bar{\Sigma}^0)$ cross sections were performed. For the detection of the Σ^0 baryon, the decay $\Sigma^0 \to \Lambda\gamma \to p\pi\gamma$ was used. About 40 candidate events were selected for the $\Sigma^0\bar{\Sigma}^0$, about 20 events for the $\Lambda\bar{\Sigma}^0$ reaction. All baryon form factors measured by BABAR have a similar size and mass shape, namely a rise towards threshold. The reason for this peculiar behaviour is not understood.

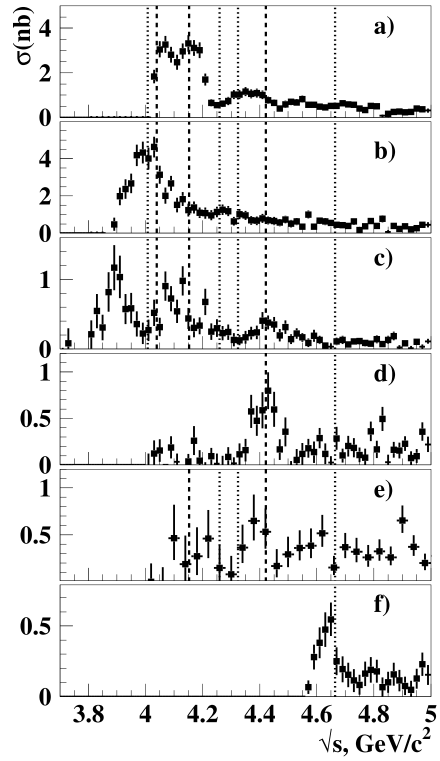

Fig. 29. Cross sections of various exclusive processes measured by Belle: a) $e^+e^- \to D\bar{D}$, b) $e^+e^- \to D^+D^{*-} + c.c.$, c) $e^+e^- \to D^{*\pm}D^{*\mp}$, d) $e^+e^- \to D^0D^-\pi^+$, e) $e^+e^- \to D^0D^{*-}\pi^+$, and f)$e^+e^- \to \Lambda_c^+\Lambda_c^-$. The dashed lines show the position of the ψ states while the dotted lines correspond to the $Y(4008)$, $Y(4260)$, $Y(4360)$, and $Y(4660)$ states.

4.4.3 Radiative return at BELLE

ISR studies at Belle

Until now most of the Belle analyses using radiative return focused on studies of the charmonium and charmonium-like states. They can be subdivided into final states with open and hidden charm.

Final states with open charm

Belle performed a systematic study of various exclusive channels of e^+e^- annihilation into charmed mesons and baryons using ISR often based on the so called partial reconstruction to increase the detection efficiency and suppress background.

In Ref. [115] they measured the cross sections of the processes $e^+e^- \to D^{*\pm}D^{*\mp}$ and $e^+e^- \to D^+D^{*-} + c.c.$. The shape of the former is complicated and has several local maxima and minima. The first two maxima are close to the $\psi(4040)$ and $\psi(4160)$ states. The latter shows significant excess of events near the $\psi(4040)$.

The cross sections of the processes $e^+e^- \to D^+D^-$ and $e^+e^- \to D^0\bar{D}^0$ show a signal of the $\psi(3770)$ as well as hints of the $\psi(4040)$, $\psi(4160)$, and $\psi(4415)$ [118]. There is also an enhancement near 3.9 GeV, which qualitatively agrees with the prediction of the coupled channel model [174].

The cross section of the process $e^+e^- \to D^0D^-\pi^+$ has a prominent peak at the energy corresponding to the $\psi(4415)$ [121]. From a study of the resonant substructure in the decay $\psi(4415) \to D^0D^-\pi^+$ they conclude that it is dominated by the intermediate $D\bar{D}_2^*(2460)$ mechanism.

In contrast to expectations of some hybrid models predicting $Y(4260) \to D^{(*)}\bar{D}^{(*)}\pi$ decays, no clear structures were observed in the cross section of the process $e^+e^- \to D^0D^{*-}\pi^+$ [175]. There is only some evidence ($\sim 3.1\sigma$) for the $\psi(4415)$.

Finally, they measure the cross section of the reaction $e^+e^- \to \Lambda_c^+\Lambda_c^-$ and observe a significant peak near threshold that they dub $X(4630)$ [122]. Assuming that the peak is a resonance, they find that its mass and width are compatible within errors with those of the $Y(4660)$ state found by Belle in the $\psi(2S)\pi^+\pi^-$ final state via ISR [117]. However, interpretations other than $X(4630) \equiv Y(4660)$ cannot be excluded. For example, peaks at the baryon-antibaryon threshold are observed in various processes [176]. According to other assumptions, the $X(4630)$ is a 5^3S_1 [177] or $\psi(6S)$ [178] charmonium state or, for example, a threshold effect, which is due to the $\psi(3D)$ slightly below the $\Lambda_c^+\Lambda_c^-$ threshold [179]. Figure 29 shows all mentioned above cross sections with the vertical lines showing positions of both well established states like $\psi(3770)$, $\psi(4040)$, $\psi(4160)$ and $\psi(4415)$ and new charmonium-like states $Y(4008)$, $Y(4260)$, $Y(4360)$ and $Y(4660)$ discussed below.

Summing the measured cross sections and taking into account not yet observed final states on base of isospin symmetry they find that until about 4.3 GeV the sum of exclusive cross sections almost saturates the total inclu-

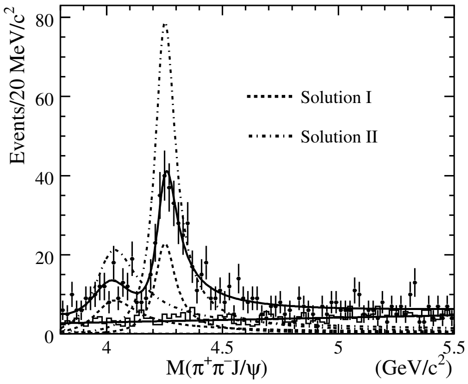

Fig. 30. The cross section of the process $e^+e^- \to J/\psi\pi^+\pi^-$

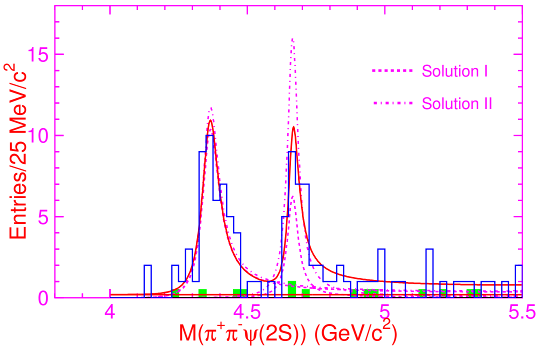

Fig. 31. The $\psi(2S)\pi^+\pi^-$ invariant mass distribution

sive cross section measured by BES [180].

Final states with hidden charm

Studying the $J/\psi\pi^+\pi^-$ final state Belle confirmed the $Y(4260)$ discovered by BaBar and in addition observed a new structure dubbed $Y(4008)$ [116], see Fig. 30. They also observe the reaction $e^+e^- \to J/\psi K^+K^-$ and find first evidence for the reaction $e^+e^- \to J/\psi K^0_S K^0_S$ [119].

Studying the $\psi(2S)\pi^+\pi^-$ final state Belle confirmed the $Y(4360)$ discovered by BaBar and in addition observed a new structure dubbed $Y(4660)$ [117], see Fig. 31.

It is worth noting that the resonance interpretation of various enhancements discussed above is not unambiguous and can be strongly affected by close thresholds of different final states and rescattering effects.

Various ISR studies performed at the Belle detector in the charmonium region are summarized in Table 2.

ISR studies of light quark states

In one case the ISR method was used to study the light quark states [181]. In this analysis the cross sections of the reactions $e^+e^- \to \phi\pi^+\pi^-$ and $e^+e^- \to \phi f_0(980)$ are measured from threshold to 3 GeV using a data sample of 673 fb^{-1}, see Fig. 32(a,b). In the $\phi\pi^+\pi^-$ mode the authors observe and measure for the first time the parameters of the $\phi(1680)$, they also observe and measure the parameters of the $\phi(2170)$. Also selected in this analysis is the $\phi f_0(980)$ final state, which shows a clear signal of the $\phi(2170)$. For Monte Carlo simulation they use a version of PHOKHARA in which the produced resonance decays into $\phi\pi^+\pi^-$ or $\phi f_0(980)$ with the subsequent decays $\phi \to K^+K^-$ and $f_0(980) \to \pi^+\pi^-$. The $\pi^+\pi^-$ system is in S-wave, the $\pi^+\pi^-$ system and the ϕ are also in a relative S-wave. The $\pi^+\pi^-$ mass distribution is generated according to phase space. They assign a 0.1% as the systematic uncertainty of the ISR photon radiator.

Table 2. Summary of ISR studies in the $c\bar{c}$ region at Belle

Final state	$\int L\ dt$, fb^{-1}	Ref.
$D^{*+}D^{*-}$	547.8	[115]
$D^{\pm}D^{*\mp}$	547.8	[115]
$D^0\bar{D}^0$, D^+D^-	673	[118]
$D^0D^-\pi^+$	673	[121]
$D^0D^{*-}\pi^+$	695	[175]
$\Lambda_c^+\Lambda_c^-$	695	[122]
$J/\psi\pi^+\pi^-$	548	[116]
$\psi(2S)\pi^+\pi^-$	673	[117]
$J/\psi K^+K^-$	673	[119]

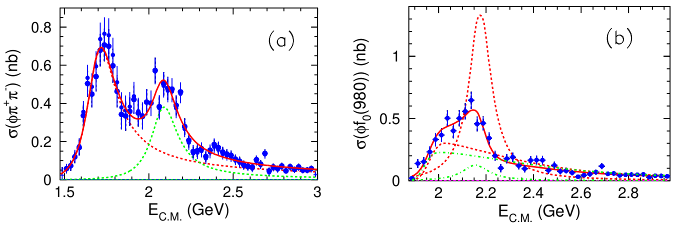

Fig. 32. The cross sections of the processes $e^+e^- \to \phi\pi^+\pi^-$ (a) and $e^+e^- \to \phi f_0(980)$ (b)

In all the ISR studies the Monte Carlo simulation is performed as follows. First, the kinematics of the initial-state radiation is generated using the PHOKHARA 5.0 package for simulation of the process $e^+e^- \to V\gamma_{\rm ISR}(\gamma_{\rm ISR})$ [32]. Then a $q\bar{q}$ generator is used to generate V decays.

4.4.4 Prospects for radiative return at VEPP2000

It is well known that the main hadronic contribution to a_μ^{had} comes from the energy region below 1 GeV and is dominated by the $\pi^+\pi^-$ channel. Direct scan experiments with CMD-3 at VEPP-2000 will deliver huge statistics, but the accuracy of the cross section determination will be determined by systematic effects. So, any other possibility to measure the pion form factor, for example with ISR, will be a valuable instrument to provide a cross check for better understanding of the systematics.

The design luminosity $\sim 10^{32}$cm^{-2}c^{-1} is expected at $\sqrt{s} = 2$ GeV. As a result, the statistics similar to that of CMD-2 will be collected. Let us recollect that the ISR method provides a "low energy scan" while data taking occurs at fixed high energy. The threshold region, $2m_\pi$–0.5 GeV, gives about 13% of the total contribution to the muon anomaly. To overcome the lack of data at threshold energies, the ISR method can serve as very efficient and unique way to measure the pion form factor.

Trigger and reconstruction efficiencies, detector imperfections will be identical for the whole energy range. As a result, some systematic errors will be canceled out at least partially and the total systematic error will be lower. Measurements of the cross section of the process $e^+e^- \to \mu^+\mu^-$ must confirm the validity of this method and will allow one to determine an energy scale and some systematic errors. A fit of the ω and ϕ resonances will also provide calibration of the energy scale. The ISR method provides an aditional instrument to better understand and estimate the systematics. Let us recollect that we are going to achieve a systematic accuracy for the pion form factor of a few pro mille.

In direct scan experiments the data as a rule are collected at fixed energy points. Thus some "empty" regions without data naturally arise. An important feature of experiments with ISR is that the whole energy scale will be covered filling any existing gaps.

Currently, the theoretical error for the cross section of the process $e^+e^- \to \pi^+\pi^-\gamma$ is dominated by the uncertainty of the radiator function (0.5%) and there is hope to reduce it to a few pro mille in future by theorists. In the case of the pion form factor extraction from the $\pi^+\pi^-\gamma/\mu^+\mu^-\gamma$ ratio, the dependence on theory will be significantly reduced since the main uncertainty of the radiator function and vacuum polarization effects cancel out in the ratio. With the integrated luminosity of several inverse femtobarn at 2 GeV one can reach a fractional accuracy on the total error better than 0.5%.

4.4.5 Prospects for radiative return at BESIII

The designed peak luminosity of the BEPCII is 1×10^{33} cm$^{-2}s^{-1}$ at $\sqrt{s} = 3.77$ GeV, i.e., the $\psi(3770)$ peak. It has reached 30% of the designed luminosity now and is starting to deliver luminosity to BESIII for physics. Although the physics programs at BESIII are rather rich [182], most of the time, the machine will run at $\sqrt{s} = 3.77$ GeV and 4.17 GeV for charm physics, since the cross sections of J/ψ and $\psi(2S)$ production are large and the required statistics can be accumulated in short time, say, one year at each energy point. An estimation of the BEPCII running time at $\sqrt{s} = 3.77$ GeV and 4.17 GeV will be around 8 years, it corresponds to an integrated luminosity of about 20 fb^{-1} at each energy point.

Data samples at $\sqrt{s} = 3.77$ GeV and 4.17 GeV can be used for radiative return study, for the center of mass energies of the hadron system between $\pi^+\pi^-$ threshold to above 2.0 GeV. This will allow a measurement of the pion form factor, the kaon form factor, and the proton form factor, as well as the cross sections of some multi-hadron final states. The good coverage of the muon detector at the BESIII also allows an identification of the $\mu^+\mu^-$ final state, thus supply as a normalization factor to the other two-body final states.

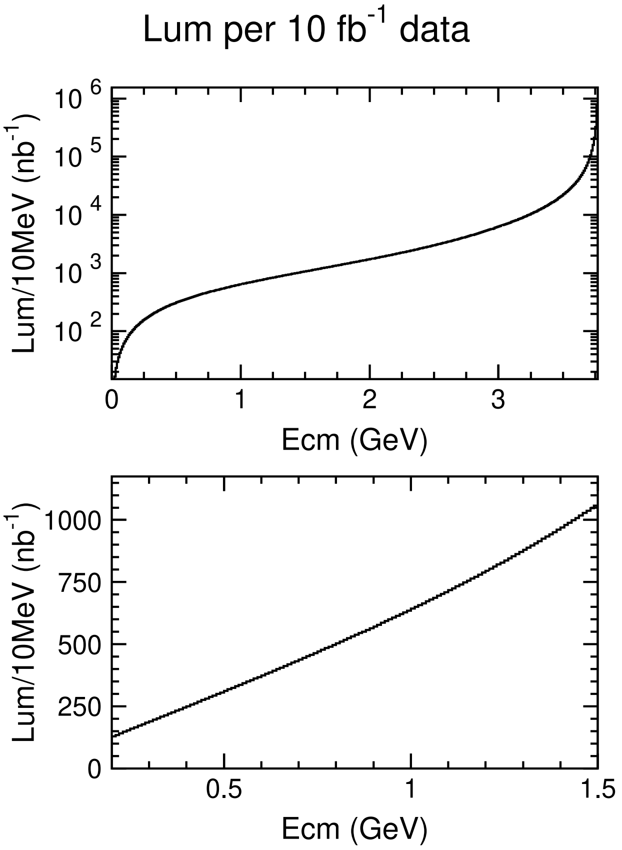

Fig. 33. Expected luminosity at low energies due to ISR for 10 fb^{-1} data accumulated on the $\psi(3770)$ peak.

Figure 33 shows the expected luminosity at low energies in 10 MeV bin for 10 fb^{-1} data accumulated on the $\psi(3770)$ peak. In terms of luminosity at the ρ^0 peak, one can see that 10 fb^{-1} data at $\sqrt{s} = 3.77$ GeV is equivalent to 70 fb^{-1} data at 10.58 GeV, namely, the B-factories.

With Monte Carlo generated $e^+e^- \to \gamma_{ISR}\pi^+\pi^-$ data using PHOKHARA [27], after a fast simulation and reconstruction with the BESIII softwares, one found the efficiency for events at the ρ^0 peak is around 5% if one requires the ISR photon is detected, this is higher than the efficiency at the BaBar experiment [183]. Figure 34 shows the signal for 10,000 generated $\pi^+\pi^-$ events. One estimates the number of events in each 10 MeV bin is around 20,000 at the ρ^0 peak for 10 fb^{-1} data at $\sqrt{s} = 3.77$ GeV. This is comparable to the recent BaBar results based on 232 fb^{-1} data at the $\Upsilon(4S)$ peak [183].

The most important work related to the pion form factor measurement is the estimation of the systematic error. Since the cross section of good events at $\psi(3770)$ peak is not large (around 30 nb for the total hadronic cross section, with about 400 nb cross section for the QED processes) compared to the highest trigger rate energies J/ψ and $\psi(2S)$ peaks, a loose trigger to allow the ISR events being recorded is out of question. In principle, the

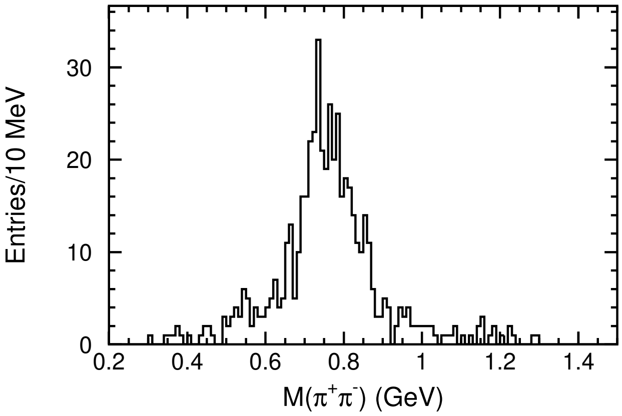

Fig. 34. Detected $\gamma_{\rm ISR}\pi^+\pi^-$ in 10000 produced events at the $\psi(3770)$ peak. The sample is generated with PHOKHARA.

trigger rate for these events could reach 100% with an allowed trigger purity of less than 20%.

With enough $D\bar{D}$ events accumulated at the same energy, the tracking efficiency and particle ID efficiency can be measured in high precision (as has been done at the CLEOc [184]); in addition, a huge data sample at $\psi(2S)$ and the well measured large branching fraction $\psi(2S)$ transition modes, such as $\pi^+\pi^- J/\psi$, $J/\psi \to \mu^+\mu^-$, can be used to study the tracking efficiency, μ-ID efficiency and so on. All these will help greatly in understanding the detector performance, and in pinning down the systematic errors in the form factor measurement.

The kaon and proton form factors can be measured as well since they are even simpler than the measurement of pion form factor. This will allow us a better understanding of the structure close to the threshold and the possible existing high mass structures.

Except for the lowest lying vector states (ρ, ω, and ϕ), the parameters of other vector states are poorly known and further investigations are needed. BESIII ISR analyses may reach a bit above 2 GeV, while above that, BEPCII can run directly by setting beam energy there. This allows BESIII a full reach of the vectors between $\pi^+\pi^-$ threshold and 4.6 GeV, the highest energy BEPCII can reach, covering the ρ, ω, ϕ, as well as the ψ sectors. Here one will have chance to study the excited ρ, ω, and ϕ states between 1 and about 2.5 GeV. The final states include $\pi^+\pi^-\pi^0$, $K\bar{K}$, 4 pions, $\pi\pi KK$, etc. Final states with more than four particles will be hard to study using ISR method, since the $D\bar{D}$ decay will contribute as background.

5 Vacuum polarization

vacuum polarization

6 Tau physics

tau physics

7 Summary

summary

References

1. C. Amsler et al. (Particle Data Group), Phys. Lett. **B667**, 1 (2008)
2. G. Balossini, C.M. Carloni Calame, G. Montagna, O. Nicrosini, F. Piccinini, Nucl. Phys. Proc. Suppl. **162**, 59 (2006), `hep-ph/0610022`
3. Nucl. Phys. Proc. Suppl. **131**, 1 (2004), Workshop on Hadronic Cross Section at Low Energy SIGHAD03; Pisa; Oct. 8-10 2003
4. Nucl. Phys. Proc. Suppl. **144**, 1 (2005), 8th Int. Workshop on Tau Lepton Physics (Tau 04); Nara; Japan; 14-17 Sept. 2004
5. Nucl. Phys. Proc. Suppl. **162**, 1 (2006), Proc. of the Int. Workshop on e+ e- Collisions from phi to psi; Novosibirsk; Feb. 27 - March 2;2006
6. Nucl. Phys. Proc. Suppl. **169**, 1 (2007), 9th Int. Workshop on Tau Lepton Physics; 19-22 September 2006; Pisa (Italy)
7. Nucl. Phys. Proc. Suppl. **181+182**, 1 (2008), Proc. of the Int. Workshop on e+ e- Collisions from Phi to Psi; Frascati 7-10 April 2008
8. Nucl. Phys. Proc. Suppl. **???**, 1 (2008), 10th Int. Workshop on Tau Lepton Physics; Novosibirsk; Russia Sept. 22-25, 2008
9. V.N. Baier, V.A. Khoze, Sov. Phys. JETP **21**, 629 (1965)
10. V.N. Baier, V.A. Khoze, Sov. Phys. JETP **21**, 1145 (1965)
11. G. Pancheri, Nuovo Cim. **A60**, 321 (1969)
12. M. Greco, G. Pancheri-Srivastava, Y. Srivastava, Nucl. Phys. **B101**, 234 (1975)
13. M.S. Chen, P.M. Zerwas, Phys. Rev. **D11**, 58 (1975)
14. S. Spagnolo, Eur. Phys. J. **C6**, 637 (1999)
15. V.A. Khoze et al., Eur. Phys. J. **C18**, 481 (2001), `hep-ph/0003313`
16. M. Benayoun, S.I. Eidelman, V.N. Ivanchenko, Z.K. Silagadze, Mod. Phys. Lett. **A14**, 2605 (1999), `hep-ph/9910523`
17. A.B. Arbuzov, E.A. Kuraev, N.P. Merenkov, L. Trentadue, JHEP **12**, 009 (1998), `hep-ph/9804430`
18. A.B. Arbuzov et al., JHEP **10**, 006 (1997), `hep-ph/9703456`
19. G. Abbiendi et al. (OPAL), Eur. Phys. J. **C33**, 173 (2004), `hep-ex/0309053`
20. J. Abdallah et al. (DELPHI), Eur. Phys. J. **C45**, 589 (2006), `hep-ex/0512012`
21. P. Achard et al. (L3), Eur. Phys. J. **C47**, 1 (2006), `hep-ex/0603022`
22. S. Schael et al. (ALEPH), Eur. Phys. J. **C49**, 411 (2007), `hep-ex/0609051`
23. S. Binner, J.H. Kühn, K. Melnikov, Phys. Lett. **B459**, 279 (1999), `hep-ph/9902399`
24. H. Czyż, J.H. Kühn, Eur. Phys. J. **C18**, 497 (2001), `hep-ph/0008262`
25. G. Rodrigo, A. Gehrmann-De Ridder, M. Guilleaume, J.H. Kühn, Eur. Phys. J. **C22**, 81 (2001), `hep-ph/0106132`

26. J.H. Kühn, G. Rodrigo, Eur. Phys. J. **C25**, 215 (2002), `hep-ph/0204283`
27. G. Rodrigo, H. Czyż, J.H. Kühn, M. Szopa, Eur. Phys. J. **C24**, 71 (2002), `hep-ph/0112184`
28. H. Czyż, A. Grzelińska, J.H. Kühn, G. Rodrigo, Eur. Phys. J. **C27**, 563 (2003), `hep-ph/0212225`
29. H. Czyż, A. Grzelińska, J.H. Kühn, G. Rodrigo, Eur. Phys. J. **C33**, 333 (2004), `hep-ph/0308312`
30. H. Czyż, A. Grzelińska, J.H. Kühn, G. Rodrigo, Eur. Phys. J. **C39**, 411 (2005), `hep-ph/0404078`
31. H. Czyż, A. Grzelińska, J.H. Kühn, Phys. Lett. **B611**, 116 (2005), `hep-ph/0412239`
32. H. Czyż, A. Grzelińska, J.H. Kühn, G. Rodrigo, Eur. Phys. J. **C47**, 617 (2006), `hep-ph/0512180`
33. H. Czyż, J.H. Kühn, A. Wapienik, Phys. Rev. **D77**, 114005 (2008), `0804.0359`
34. H. Czyż, J.H. Kühn, E. Nowak, G. Rodrigo, Eur. Phys. J. **C35**, 527 (2004), `hep-ph/0403062`
35. H. Czyż, A. Grzelińska, J.H. Kühn, Phys. Rev. **D75**, 074026 (2007), `hep-ph/0702122`
36. H. Czyż, A. Grzelińska, A. Wapienik, Acta Phys. Polon. **B38**, 3491 (2007), `0710.4227`
37. H. Czyż, Nucl. Phys. Proc. Suppl. **162**, 76 (2006), `hep-ph/0606227`
38. H. Czyż, Nucl. Phys. Proc. Suppl. **181-182**, 264 (2008)
39. A. Grzelińska, H. Czyż, A. Wapienik (2008), `0812.1939`
40. M. Caffo, H. Czyż, E. Remiddi, Phys. Lett. **B327**, 369 (1994)
41. K. Melnikov, F. Nguyen, B. Valeriani, G. Venanzoni, Phys. Lett. **B477**, 114 (2000), `hep-ph/0001064`
42. S. Dubinsky, A. Korchin, N. Merenkov, G. Pancheri, O. Shekhovtsova, Eur. Phys. J. **C40**, 41 (2005), `hep-ph/0411113`
43. G. Pancheri, O. Shekhovtsova, G. Venanzoni, Phys. Lett. **B642**, 342 (2006), `hep-ph/0605244`
44. G. Pancheri, O. Shekhovtsova, G. Venanzoni, J. Exp. Theor. Phys. **106**, 470 (2008), `0706.3027`
45. O. Shekhovtsova, G. Venanzoni, G. Pancheri, Comput. Phys. Commun. **180**, 1206 (2009), `0901.4440`
46. G. Cataldi, A. Denig, S. Müller, W. Kluge, G. Venanzoni (1999), KLOE memo 195 (Aug. 1999), Frascati Physics Series (2000) 569
47. A. Denig et al. (KLOE) (2001), `hep-ex/0106100`
48. A. Aloisio et al. (KLOE) (2001), `hep-ex/0107023`
49. A.G. Denig et al. (the KLOE), Nucl. Phys. Proc. Suppl. **116**, 243 (2003), `hep-ex/0211024`
50. B. Valeriani et al. (KLOE) (2002), `hep-ex/0205046`
51. G. Venanzoni et al. (KLOE), Nucl. Phys. Proc. Suppl. **123**, 177 (2003), `hep-ex/0210013`
52. S.E. Müller (KLOE), Nucl. Phys. Proc. Suppl. **126**, 335 (2004)
53. A. Aloisio et al. (KLOE), Eur. Phys. J. **C33**, s656 (2004), `hep-ex/0307051`
54. A.G. Denig (KLOE), AIP Conf. Proc. **717**, 83 (2004), `hep-ex/0311012`
55. B. Valeriani (KLOE), Nucl. Phys. Proc. Suppl. **131**, 75 (2004)
56. W. Kluge, Nucl. Phys. Proc. Suppl. **135**, 357 (2004)
57. A.G. Denig (KLOE), Int. J. Mod. Phys. **A20**, 1935 (2005)
58. W. Kluge (KLOE), Acta Physica Slovaca **55**, 49 (2005)
59. A. Aloisio et al. (KLOE), Nucl. Phys. Proc. Suppl. **144**, 231 (2005)
60. A. Denig, Nucl. Phys. Proc. Suppl. **162**, 81 (2006), `hep-ex/0611024`
61. S.E. Müller, F. Nguyen (KLOE), Nucl. Phys. Proc. Suppl. **162**, 90 (2006)
62. D. Leone (KLOE), Nucl. Phys. Proc. Suppl. **162**, 95 (2006)
63. G. Venanzoni (KLOE), Nucl. Phys. Proc. Suppl. **169**, 277 (2007)
64. F. Nguyen (KLOE), Nucl. Phys. Proc. Suppl. **181-182**, 106 (2008), `0807.1612`
65. S.E. Müller (KLOE), Acta Phys. Polon. **B38**, 3007 (2007)
66. F. Ambrosino et al. (KLOE) (2007), `0707.4078`
67. A. Aloisio et al. (KLOE), Phys. Lett. **B606**, 12 (2005), `hep-ex/0407048`
68. F. Ambrosino et al. (KLOE), Phys. Lett. **B670**, 285 (2009), `0809.3950`
69. W. Kluge, Nucl. Phys. Proc. Suppl. **181-182**, 280 (2008), `0805.4708`
70. G. Venanzoni (for the KLOE Collaboration) (2009), `0906.4331`
71. G.W. Bennett et al. (Muon g-2), Phys. Rev. Lett. **89**, 101804 (2002), `hep-ex/0208001`
72. G.W. Bennett et al. (Muon g-2), Phys. Rev. Lett. **92**, 161802 (2004), `hep-ex/0401008`
73. G.W. Bennett et al. (Muon G-2), Phys. Rev. **D73**, 072003 (2006), `hep-ex/0602035`
74. D.W. Hertzog, Nucl. Phys. Proc. Suppl. **181-182**, 5 (2008)
75. F. Jegerlehner, *The anomalous magnetic moment of the muon*, Berlin, Germany: Springer 426 p (2008)
76. M. Davier, W.J. Marciano, Ann. Rev. Nucl. Part. Sci. **54**, 115 (2004)
77. T. Teubner, Nucl. Phys. Proc. Suppl. **181-182**, 20 (2008)
78. F. Jegerlehner, Nucl. Phys. Proc. Suppl. **181-182**, 26 (2008)
79. St (????)
80. J.H. Kühn, M. Steinhauser, Phys. Lett. **B437**, 425 (1998), `hep-ph/9802241`
81. S. Eidelman, F. Jegerlehner, A.L. Kataev, O. Veretin, Phys. Lett. **B454**, 369 (1999), `hep-ph/9812521`
82. K.G. Chetyrkin, J.H. Kühn, A. Kwiatkowski, Phys. Rept. **277**, 189 (1996)
83. R.R. Akhmetshin et al. (CMD-2), Phys. Lett. **B527**, 161 (2002), `hep-ex/0112031`
84. R.R. Akhmetshin et al., Phys. Lett. **B551**, 27 (2003), `hep-ex/0211004`
85. R.R. Akhmetshin et al. (CMD-2), Phys. Lett. **B562**, 173 (2003), `hep-ex/0304009`
86. R.R. Akhmetshin et al. (CMD-2), Phys. Lett. **B578**, 285 (2004), `hep-ex/0308008`
87. V.M. Aulchenko et al. (CMD-2), JETP Lett. **82**, 743 (2005), `hep-ex/0603021`
88. R.R. Akhmetshin et al. (CMD2), Phys. Lett. **B605**, 26 (2005), `hep-ex/0409030`
89. R.R. Akhmetshin et al., JETP Lett. **84**, 413 (2006), `hep-ex/0610016`
90. F. Ignatov (CMD-2 and SND), Nucl. Phys. Proc. Suppl. **181-182**, 101 (2008)
91. R.R. Akhmetshin et al. (CMD-2), Phys. Lett. **B648**, 28 (2007), `hep-ex/0610021`
92. M.N. Achasov et al., Phys. Rev. **D68**, 052006 (2003), `hep-ex/0305049`

93. M.N. Achasov et al., J. Exp. Theor. Phys. **101**, 1053 (2005), hep-ex/0506076
94. M.N. Achasov et al., Nucl. Phys. Proc. Suppl. **162**, 11 (2006), hep-ex/0604052
95. M.N. Achasov et al., J. Exp. Theor. Phys. **103**, 380 (2006), hep-ex/0605013
96. M.N. Achasov et al., Phys. Rev. **D76**, 072012 (2007), 0707.2279
97. M.N. Achasov et al., J. Exp. Theor. Phys. **103**, 720 (2006), hep-ex/0606057
98. M. Davier et al. (2009), 0906.5443
99. E.P. Solodov (BABAR) (2002), hep-ex/0107027
100. B. Aubert et al. (BABAR), Phys. Rev. **D69**, 011103 (2004), hep-ex/0310027
101. B. Aubert et al. (BABAR), Phys. Rev. **D70**, 072004 (2004), hep-ex/0408078
102. B. Aubert et al. (BABAR), Phys. Rev. **D71**, 052001 (2005), hep-ex/0502025
103. B. Aubert et al. (BABAR), Phys. Rev. **D73**, 012005 (2006), hep-ex/0512023
104. B. Aubert et al. (BABAR), Phys. Rev. **D73**, 052003 (2006), hep-ex/0602006
105. B. Aubert et al. (BABAR), Phys. Rev. **D74**, 091103 (2006), hep-ex/0610018
106. B. Aubert et al. (BABAR), Phys. Rev. **D76**, 012008 (2007), 0704.0630
107. B. Aubert et al. (BaBar), Phys. Rev. **D77**, 092002 (2008), 0710.4451
108. B. Aubert et al. (BABAR), Phys. Rev. **D76**, 092005 (2007), 0708.2461
109. B. Aubert et al. (BABAR), Phys. Rev. **D76**, 092006 (2007), 0709.1988
110. B. Aubert et al. (BABAR), Phys. Rev. **D76**, 111105 (2007), hep-ex/0607083
111. B. Aubert et al. (BaBar) (2008), 0808.1543
112. B. Aubert et al. (BABAR) (2009), 0903.1597
113. A.G. Denig, P.A. Lukin (BABAR), Nucl. Phys. Proc. Suppl. **181-182**, 111 (2008)
114. M. Davier (2009), to be published in Nucl. Phys. **B**, Proc. Suppl.(2009), http://tau08.inp.nsk.su/prog.php
115. K. Abe et al. (Belle), Phys. Rev. Lett. **98**, 092001 (2007), hep-ex/0608018
116. C.Z. Yuan et al. (Belle), Phys. Rev. Lett. **99**, 182004 (2007), 0707.2541
117. X.L. Wang et al. (Belle), Phys. Rev. Lett. **99**, 142002 (2007), 0707.3699
118. G. Pakhlova et al. (Belle), Phys. Rev. **D77**, 011103 (2008), 0708.0082
119. C.Z. Yuan et al. (Belle), Phys. Rev. **D77**, 011105 (2008), 0709.2565
120. G. Pakhlova, Nucl. Phys. Proc. Suppl. **181-182**, 117 (2008)
121. G. Pakhlova et al. (Belle), Phys. Rev. Lett. **100**, 062001 (2008), 0708.3313
122. G. Pakhlova et al. (Belle), Phys. Rev. Lett. **101**, 172001 (2008), 0807.4458
123. B. Aubert et al. (BABAR), Phys. Rev. Lett. **95**, 142001 (2005), hep-ex/0506081
124. E. Prencipe, Nucl. Phys. Proc. Suppl. **181-182**, 333 (2008)
125. K. Abe et al. (Belle) (2006), hep-ex/0612006
126. V. Balagura (Belle), Nucl. Phys. Proc. Suppl. **181-182**, 338 (2008)
127. T.E. Coan et al. (CLEO), Phys. Rev. Lett. **96**, 162003 (2006), hep-ex/0602034
128. Q. He et al. (CLEO), Phys. Rev. **D74**, 091104 (2006), hep-ex/0611021
129. Y.S. Kalashnikova, Nucl. Phys. Proc. Suppl. **181-182**, 363 (2008)
130. F.E. Maas (PANDA), Nucl. Phys. Proc. Suppl. **181-182**, 45 (2008)
131. G. Salme, Nucl. Phys. Proc. Suppl. **181-182**, 51 (2008), 0807.0344
132. V.F. Dmitriev, A.I. Milstein, Nucl. Phys. Proc. Suppl. **181-182**, 66 (2008)
133. R. Baldini, S. Pacetti, A. Zallo, A. Zichichi, Eur. Phys. J. **A39**, 315 (2009), 0711.1725
134. J. Arrington, Phys. Rev. **C68**, 034325 (2003), nucl-ex/0305009
135. G. Rodrigo, Acta Phys. Polon. **B32**, 3833 (2001), hep-ph/0111151
136. M. Caffo, H. Czyż, E. Remiddi, Nuovo Cim. **A110**, 515 (1997), hep-ph/9704443
137. F.A. Berends, K.J.F. Gaemer, R. Gastmans, Nucl. Phys. **B57**, 381 (1973)
138. F.A. Berends, W.L. van Neerven, G.J.H. Burgers, Nucl. Phys. **B297**, 429 (1988)
139. J.S. Schwinger (1989), Particles, Sources, and Fields. Vol. 3, Redwood City, USA: Addison-Wesley (1989), p.99
140. A. Hoefer, J. Gluza, F. Jegerlehner, Eur. Phys. J. **C24**, 51 (2002), hep-ph/0107154
141. F. Jegerlehner, K. Kolodziej, Eur. Phys. J. **C12**, 77 (2000), hep-ph/9907229
142. K. Kolodziej, M. Zralek, Phys. Rev. **D43**, 3619 (1991)
143. H. Czyż, E. Nowak-Kubat, Phys. Lett. **B634**, 493 (2006), hep-ph/0601169
144. H. Czyż, E. Nowak-Kubat, Acta Phys. Polon. **B36**, 3425 (2005), hep-ph/0510287
145. S. Jadach, B.F.L. Ward, S.A. Yost, Phys. Rev. **D73**, 073001 (2006), hep-ph/0602197
146. C. Glosser, S. Jadach, B.F.L. Ward, S.A. Yost, Phys. Lett. **B605**, 123 (2005), hep-ph/0406298
147. R. Tarrach, Nuovo Cim. **A28**, 409 (1975)
148. D. Drechsel, G. Knochlein, A. Metz, S. Scherer, Phys. Rev. **C55**, 424 (1997), nucl-th/9608061
149. G. Ecker, J. Gasser, H. Leutwyler, A. Pich, E. de Rafael, Phys. Lett. **B223**, 425 (1989)
150. G. Ecker, J. Gasser, A. Pich, E. de Rafael, Nucl. Phys. **B321**, 311 (1989)
151. N.N. Achasov, V.V. Gubin, E.P. Solodov, Phys. Rev. **D55**, 2672 (1997), hep-ph/9610282
152. N.N. Achasov, A.V. Kiselev, Phys. Rev. **D73**, 054029 (2006), hep-ph/0512047
153. O. Shekhovtsova, http://ific.uv.es/~rodrigo/phokhara/, (2008),PHOKHARA6.1, unpublished
154. F. Ambrosino et al. (KLOE), Eur. Phys. J. **C49**, 473 (2007), hep-ex/0609009
155. P. Beltrame, *Measurement of the pion form factor via Radiative Return for $\sqrt{s}$ = 1 GeV with the KLOE detector*, PhD thesis, KA-IEKP-2009-8 (2009)
156. D. Leone, *Measurement of the hadronic cross section sigma(e+ e- → pi+ pi-) with the KLOE detector using radiative return with tagged photons*, PhD thesis, KA-IEKP-2007-7 (2007)
157. C. Bruch, A. Khodjamirian, J.H. Kuhn, Eur. Phys. J. **C39**, 41 (2005), hep-ph/0409080

158. J.H. Kuhn, A. Santamaria, Z. Phys. **C48**, 445 (1990)
159. S. Eidelman, F. Jegerlehner, Z. Phys. **C67**, 585 (1995), hep-ph/9502298
160. F. Ambrosino et al. (KLOE), Phys. Lett. **B670**, 285 (2009), 0809.3950
161. C.M. Carloni Calame, C. Lunardini, G. Montagna, O. Nicrosini, F. Piccinini, Nucl. Phys. **B584**, 459 (2000), hep-ph/0003268
162. G. Balossini, C.M. Carloni Calame, G. Montagna, O. Nicrosini, F. Piccinini, Nucl. Phys. **B758**, 227 (2006), hep-ph/0607181
163. F. Jegerlehner, http://www-com.physik.hu-berlin.de/~fjeger/alphaQED.uu, fortran code for the effective fine structure constant
164. H. Czyż et al., unpublished
165. S. Mueller et al., http://www.lnf.infn.it/kloe/pub/knote/kn221.pdf
166. F. Ambrosino et al., Nucl. Instrum. Meth. **A534**, 403 (2004), physics/0404100
167. A. Denig et al., http://www.lnf.infn.it/kloe/pub/knote/kn192.ps
168. A. Bramon, G. Colangelo, P.J. Franzini, M. Greco, Phys. Lett. **B287**, 263 (1992)
169. J.L. Lucio Martinez, M. Napsuciale, Phys. Lett. **B331**, 418 (1994)
170. M.N. Achasov et al. (SND), Preprint Budker INP 2001-34 (2001)
171. P.L. Frabetti et al. (E687), Phys. Lett. **B514**, 240 (2001), hep-ex/0106029
172. G. Bardin et al., Nucl. Phys. **B411**, 3 (1994)
173. D. Bisello et al. (DM2), Z. Phys. **C48**, 23 (1990)
174. E. Eichten, K. Gottfried, T. Kinoshita, K.D. Lane, T.M. Yan, Phys. Rev. **D21**, 203 (1980)
175. G. Pakhlova (Belle) (2009), 0908.0231
176. K. Abe et al. (Belle), Phys. Rev. Lett. **88**, 181803 (2002), hep-ex/0202017
177. A.M. Badalian, B.L.G. Bakker, I.V. Danilkin, Phys. Atom. Nucl. **72**, 638 (2009), 0805.2291
178. B.Q. Li, K.T. Chao, Phys. Rev. D **79**, 094004 (2009), 0903.5506
179. E. van Beveren, X. Liu, R. Coimbra, G. Rupp (2008), 0809.1151
180. J.Z. Bai et al. (BES), Phys. Rev. Lett. **88**, 101802 (2002), hep-ex/0102003
181. I. Adachi et al. (Belle) (2008), 0808.0006
182. D.M. Asner et al. (2008), 0809.1869
183. L. Wang, Ph.D. thesis, Institute of High Energy Physics, Chinese Academy of Sciences, and Laboratoire de l'Accelerateur Lineaire, Universite Paris-Sud 11 (2009)
184. S. Dobbs et al. (CLEO), Phys. Rev. **D76**, 112001 (2007), 0709.3783